Thermodynamic modeling and experimental study of carbonation of alkali activated slag cements

Solmoi Park[a,b,c,*], Barbara Lothenbach[c,d], Jeong Gook Jang[e,*], Hyeong-Ki Kim[f], Namkon Lee[g]

[a] Department of Civil Engineering, Pukyong National University,
45 Yongso-ro, Nam-gu, 48513 Busan, Republic of Korea

[b] Department of Civil and Environmental Engineering,
Korea Advanced Institute of Science and Technology (KAIST),
291 Daehak-ro, Yuseong-gu, 34141 Daejeon, Republic of Korea

[c] Laboratory for Concrete & Construction Chemistry, Swiss Federal Laboratories for
Materials Science and Technology (Empa), 8600 Dübendorf, Switzerland
Barbara.Lothenbach@empa.ch

[d] Department of Structural Engineering,
Norwegian University of Science and Technology (NTNU),
7491 Trondheim, Norway

[e] Division of Architecture and Urban Design, Institute of Urban Science,
Incheon National University,
119 Academy-ro, Yeonsu-gu, 22012 Incheon, Republic of Korea

[f] School of Architecture, Chosun University,
309 Pilmun-daero, Dong-gu, 61452 Gwangju, Republic of Korea
hyeongki@chosun.ac.kr

[g] Structural Engineering Research Division,
Korea Institute of Civil Engineering and Building Technology,
283 Goyangdae-ro, Ilsanseo-gu, Goyang-si, 10223 Gyeonggi-Do, Republic of Korea
nklee@kict.re.kr

Corresponding authors:
solmoi.park@pknu.ac.kr (S.P.)
jangjg@inu.ac.kr (J.G.J.)

Abstract

The present study investigates the carbonation of slags activated by NaOH, Na_2SiO_3, Na_2CO_3 and Na_2SO_4. The main hydrates in those activated with NaOH or Na_2SiO_3 were C-(N-)A-S-H, strätlingite and MgAl-layered double hydroxide phases as observed using different experimental characterizations techniques and thermodynamic modeling. The use of a Na_2CO_3 activator led to the formation of calcium carbonate and monocarbonate instead of strätlingite, and Na_2SO_4 to ettringite formation. Carbonation of the alkali-activated slags in a powdered form at 1 vol.% concentration of CO_2 environment proceeded rapidly, where little change was observed after 7 d. The main carbonation products commonly identified were calcium carbonate, carbonate containing-MgAl-layered double hydroxide, and N-A-S-H. In Na_2SiO_3- and Na_2SO_4-activated slags M-S-H formation was predicted, which destabilized the MgAl-layered double hydroxide phases. Strätlingite and monocarbonate, which were initially present or formed as a transient phase, were transformed to N-A-S-H during carbonation, while C-(N-)A-S-H was only partially decalcified and destabilized.

Keywords: Alkali Activated Cement; Granulated Blast-Furnace Slag; Carbonation; Thermodynamic Modeling

Introduction

In recent years use of cementitious binders alternative to Portland cement has become necessary to mitigate the environmental CO_2 footprint associated with Portland cement production [1-3]. Alkali-activated cements are one of alternative cementitious binders that are being extensively investigated due to its lower footprint compared to Portland cement [4-6]. Among the binders that can be used in alkali-activated cements, granulated blast furnace slag (hereafter referred to as 'slag') has been a topic of many studies over the past decades. The annual global output of steel slag is reported to be ~1600 million tons [7, 8], and granulated blast furnace slag accounts for 300~360 million tons and is nearly fully used as a supplementary cementitious material in concrete production [9]. NaOH and Na_2SiO_3 have been frequently used as an activator [10-12], and other alkali sources (e.g., Na_2CO_3 and Na_2SO_4) are also used to achieve the required functional properties. Slags activated with NaOH or Na_2SiO_3 have been broadly discussed in a vast number of studies, which revealed many important aspects of kinetics of alkali-activation and the reaction products formed from experimental and theoretical investigations [6, 13-17]. Less is known about slag activated with Na_2CO_3 and Na_2SO_4; only a few experimental [18-22] and modeling studies [23] are available in the literature. In particular, their durability performance needs to be better understood.

Carbonation is a degradation mechanism that leads to a structural alteration in the hydration products and to which alkali-activated slag is particularly susceptible [10]. This is a major drawback of alkali-activated slag cements, which typically exhibit outstanding durability performance (i.e., against as sulfate and acid attack), in comparison with Portland cement-based systems [24, 25]. Carbonation neutralizes the pore solution and can lead to corrosion of embedded rebars for concrete; for alkali-activated slags it can cause a reduction in the compressive strength [10, 26]. The weak resistance of alkali-activated slag against carbonation can

be attributed to the absence of portlandite in contrast to hydrated Portland cement [27, 28]. A high alkali dosage may improve the carbonation resistance of alkali-activated slag by enhancing the slag reaction and reducing the porosity [29].

Another issue of the carbonation of alkali-activated slag is related to the difference in carbonation behavior in a testing environment compared to natural carbonation. It has been observed that the carbonation performance of alkali-activated slag is notably underestimated when tested under accelerated high CO_2 concentrations [24, 30]. This phenomenon limits not only the use of experimental data obtained under accelerated conditions for understanding the carbonation of alkali-activated slag, but also does not allow quantitative comparison of its performance with the data for Portland cement-based systems widely available in literature.

This study investigates the carbonation of alkali-activated slag activated with four different Na-based activators, including NaOH and Na_2SiO_3, Na_2CO_3 and Na_2SO_4. Samples were carbonated at a low CO_2 concentration (i.e., 1%). The obtained experimental data were complemented with thermodynamic calculations to provide in-depth information regarding hydration and carbonation of alkali-activated slag samples that are produced from various activators.

Materials and methods

Sample preparation

Alkali-activated slag samples were produced by mixing blast furnace slag with NaOH (supplied by Daejung, pellets, 98% purity), $Na_2SiO_3 \cdot 5.3H_2O$ (supplied by Honam Chemical Inc.), Na_2CO_3 (supplied by Samchun, 99% purity), or Na_2SO_4 (supplied by Daejung, 99% purity). The chemical composition of the slag as determined by X-ray fluorescence is provided in Table 1. The Baline specific surface and the specific gravity of the slag were 4100 cm^2/g and 2.9, respectively.

The activator dosage was 10 g per 100 g of slag, and water/binder (activator + slag) ratio was 0.495 in all samples, corresponding to water/slag = 0.45 (Table 2), for simplicity in practical uses. This resulted in Na_2O dosages of 7.75, 5.08, 5.85 and 4.36 g per 100 g of slag for NaOH, Na_2SiO_3, Na_2CO_3 and Na_2SO_4, respectively. In the case where $Na_2SiO_3 \cdot 5.3H_2O$ was used, the activator dosage and the total H_2O were adjusted to incorporate 10 g Na_2SiO_3 and to consider the molecular water of this activator, respectively. The samples were prepared at room temperature and were cured at 25 °C and 100% relative humidity for 50 d prior to carbonation.

Table 1. Chemical composition of blast furnace slag (mass-%)

CaO	SiO$_2$	Al$_2$O$_3$	Fe$_2$O$_3$	MgO	Na$_2$O	K$_2$O	SO$_3$	TiO$_2$	P$_2$O$_5$	Mn$_2$O$_3$	SrO	LOI*
43.61	36.18	14.15	0.31	3.46	0.22	0.53	0.37	0.67	0.02	0.37	0.07	0.03

* Loss on ignition, determined in accordance with ASTM C114.

Table 2. Mixture proportions

Activator used	Slag (g)	Activator (g)	Water (g)	Water/binder
NaOH	100	10.0	45.0	0.450
Na$_2$SiO$_3 \cdot$5.3H$_2$O	100	10.0	40.6	0.406
Na$_2$CO$_3$	100	10.0	45.0	0.450
Na$_2$SO$_4$	100	10.0	45.0	0.450

Carbonation of samples

After 50 d of curing, the samples were manually ground with a mortar and pestle to pass a 100 μm sieve, allowing carbonation to occur uniformly in the samples and reduce sampling errors. The powdered samples were uniformly dispersed in a tray and placed in a carbonation chamber. The carbonation conditions involved 1 vol.% concentration of CO_2, 25 °C and 60±5% relative humidity, which were maintained by using the chamber.

Characterization

Hydration stoppage by solvent exchange was applied to the samples prior to characterization. The obtained samples were characterized by X-ray diffraction (XRD), thermogravimetric analysis (TGA) and solid-state magic angle spinning nuclear magnetic resonance (MAS NMR) spectroscopy.

XRD patterns for the samples were obtained across a 2θ range of 5-65 ° using an X'Pert Pro X-ray diffractometer (Malvern Panalytical) and a Pixel and X'Celator detector at 30 mA and 40 kV, with CuKα radiation and a step size of 0.026 ° 2θ. Each sample was scanned for 30 min.

TGA was conducted using a TA Instruments Q600 at a heating rate of 10 °C/min from 40 to 800 °C in N_2 gas. The mass of CO_2 gas released from the samples during TGA was calculated from derivative thermograms (DTG) by integrating the area of the corresponding mass loss hump under an appropriate baseline (i.e., tangential method). The start and end points of the mass loss hump due to decarbonation were manually selected for integration. The integrated areas were divided by the final residual mass to normalize the values to 100 g anhydrous slag. The amount of CO_2 that was introduced by the use of activator (Na_2CO_3) was excluded from the CO_2 uptake of the samples by subtracting the mass of CO_2 supplied by Na_2CO_3 per 100 g slag, otherwise, the mass of CO_2 obtained by the tangential method was used.

Solid-state ^{27}Al and ^{29}Si MAS NMR spectra were obtained using an Avance III HD

instrument (9.4T, Bruker). ^{27}Al MAS NMR spectra were acquired at a Lamor frequency of 104.29 MHz, spinning rate of 14 kHz, relaxation delay of 2 s, and pulse length of 1.2 μs. ^{29}Si MAS NMR spectra were acquired at a Lamor frequency of 79.51 MHz, spinning rate of 11 kHz, relaxation delay of 20 s, and pulse length of 1.6 μs. The chemical shifts were referenced to $AlCl_3$ at 0 ppm and TMS at 0 ppm for ^{27}Al and ^{29}Si MAS NMR spectroscopy, respectively.

The obtained ^{29}Si MAS NMR spectra were decomposed into simulated peaks using OriginPro by introducing a minimum number of Gaussian peaks at the chemical shifts at which the reaction and carbonation products are known to resonate [28, 31-33]. The experimental spectra were simulated using a minimum number of peaks. The resonance of the anhydrous slag in the spectra of the raw slag and hydrated samples was simulated by a single peak using the Gaussian LorenCross function. The fitting parameters (center, width, peak shape and amplitude) were obtained from the raw slag spectrum. The values of the parameters were kept identical except for the amplitude for simulating the anhydrous slag resonance in the hydrated samples. The mean chain length (MCL) of calcium-(sodium-)aluminosilicate-hydrate (C-(N-)A-S-H) was calculated using the cross-linked substituted tobermorite model [34].

Thermodynamic modeling

Thermodynamic modeling was performed using the Gibbs free energy minimization software GEM-Selektor v.3.5 [35, 36] and CEMDATA18 [37], which contains a database for the thermodynamic properties of phases encountered in hydrated cementitious binders. Highly-crosslinked alkali aluminosilicate (N-A-S-H) gels that substantially form upon carbonation of C-(N-)A-S-H were modeled using thermodynamic data for N-A-S-H 1 and N-A-S-H 2 reported in [38]. The database was completed with additional data for magnesium-silicate-hydrate (M-S-H) with aluminum using the thermodynamic data published by Bernard et al. [39], sodium carbonates, such as nahcolite ($NaHCO_3$), natron ($Na_2CO_3 \cdot 10H_2O$), thermonatrite

($Na_2CO_3 \cdot H_2O$), trona ($Na_2CO_3 \cdot NaHCO_3 \cdot 2H_2O$) [40] and gaylussite ($Na_2Ca(CO_3)_2 \cdot 5H_2O$) [41], and carbonate containing hydrotalcites [42].

The activity coefficients for aqueous species were calculated using the Truesdell-Jones extension to the Debye–Hückel equation [43], given as follows:

$$log_{10}\gamma_i = \frac{-A_\gamma z_i^2 \sqrt{I}}{1 + \dot{a}B_\gamma \sqrt{I}} + b_\gamma I + log_{10}\frac{X_{jw}}{X_w}$$

Equation 1

where γ_i and z_i are the activity coefficient and charge of the ith species, respectively. A_γ and B_γ are temperature- and pressure-dependent coefficients, respectively. I is the effective molal ionic strength. X_{jw} and X_w are the molar quantity of water and total molar amount of the aqueous phase, respectively. $\dot{a}$ and b_γ are a common ion size parameter and short-range interaction parameter, respectively, and were set to 3.31 Å and 0.098 kg/mol, using NaOH as the background electrolyte.

The thermodynamic calculations were carried out by assuming a congruent dissolution of the slag. The reaction degree of the slag obtained from the spectral deconvolution of the ^{29}Si MAS NMR spectra and the CO_2 uptake in the samples measured by TGA at the corresponding test days shown in Figure 1 were used to simulate the phase assemblage of the samples as a function of carbonation time. The atmospheric concentration of CO_2 in the simulation was kept identical to the experimental condition (1%) by introducing O_2 in the simulated atmosphere.
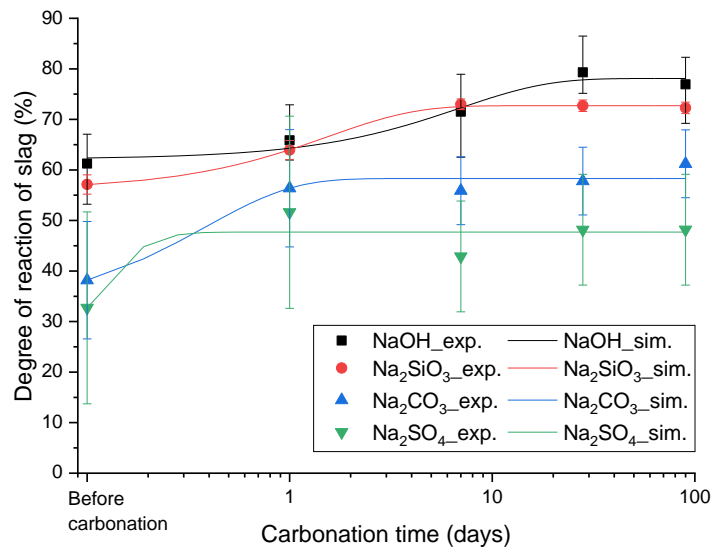
(a)
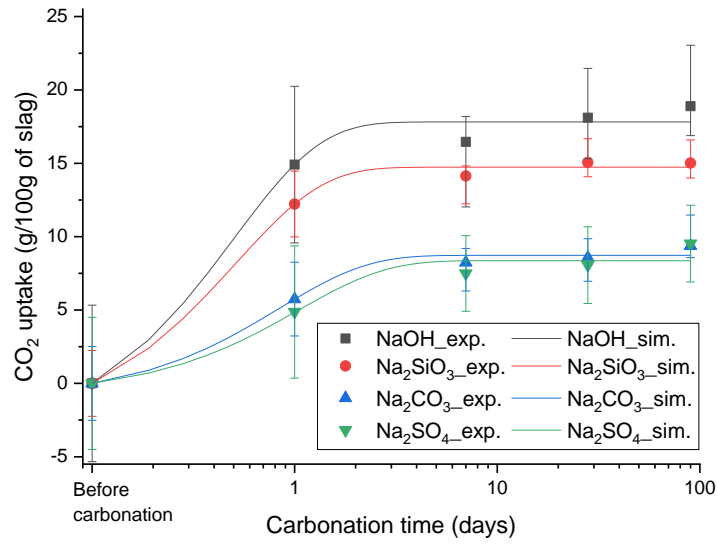
(b)

Figure 1. Experimental (dots) and simulated (lines) (a) CO_2 uptake per 100g of slag and (b) a degree of reaction of slag as a function of carbonation time. Error bars indicate the 95% confidence interval of the simulated lines. The lines were fitted using $y = a * \exp(t/b) + c$, where y is the degree of reaction of slag or CO_2 uptake, t is the carbonation time in days, and a, b and c are constants.

Results

The TGA data show that for all the samples, regardless of the activator used, a relatively fast uptake of CO_2 is observed during the first days as the use of finely ground hydrated samples resulted in a relatively fast and uniform carbonation (Figure 1 (a)). The Na_2SO_4- and Na_2CO_3 activated samples exhibit a total CO_2 uptake of approximately 10 g/ 100 g unreacted slag, while the Na_2SiO_3– and the NaOH–activated slag show CO_2 uptakes of 15 g/100 g and 19 g/100 g, respectively, which is related to both the different degrees of slag reaction and different chemistries depending on the activator used. These values are comparable or higher than that of hydrated neat and blended Portland cement carbonated in a natural condition for a few years[44]. It is possible that the high alkalinity of the NaOH activator as compared to the other activators may lead to higher reaction degree of slag. It is known that hydrotalcite-like LDH is less stable in the presence of sodium silicate [23], thus use of Na_2SiO_3 as an activator may lead to increasing the carbonation extent.

The deconvolution of the NMR data of the hydrated samples illustrates after 50 d of hydration, a slag reaction of approximately 60% for the NaOH– and Na_2SiO_3–activated samples and between 30 and 40% for the Na_2SO_4 and Na_2CO_3 activators (Figure 1 (b)). The data summarized in Figure 1 (b) also show that the slag continues to react during carbonation. The slag reaction increases by at least 15% for all activators during carbonation, and the Na_2CO_3 activated samples experience more than a 20% increase after 90 d of carbonation. The progress of slag hydration as a function of carbonation time was described using the following empirical equation, which allows interpolation of the results.

$$y = a\,e^{(t/b)} + c \hspace{4cm} \text{Equation 2}$$

where, y is either CO_2 uptake or reaction degree of slag (g/100g slag), t is carbonation time in

days, and a, b and c are constant. Despite that the overall fitting resulted in a minimum R^2 value of 0.96, the slag reaction for the Na_2SO_4 sample was particularly high after 1 d of carbonation, which resulted in a higher error margin up to 19%.

Thermodynamic modeling was used to predict the composition of the hydrated slag and its expected changes during carbonation. The hydrated phase assemblage in Figure 2 was predicted based on the experimentally measured slag reaction degree and CO_2 uptake after 1, 7, 28, and 90 d of carbonation at 1% CO_2 concentration (see Figure 1). It is predicted that C-(N-)A-S-H, strätlingite, LDH, and katoite would be the stable phases in NaOH–activated slag before carbonation. The amount of strätlingite predicted using the modeling may have been overestimated, because it is not identified in XRD patterns of alkali–activated slags [4, 45]. A thermodynamic modeling study by Myers et al. [13] suggests that the source of this error can be due to another phase (zeolites or geopolymer gels) missing in the database, which preferentially forms over strätlingite.
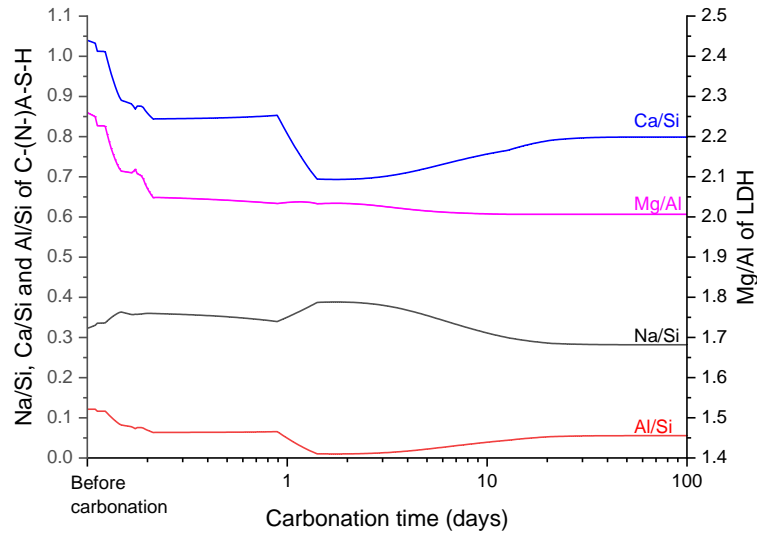
(a)
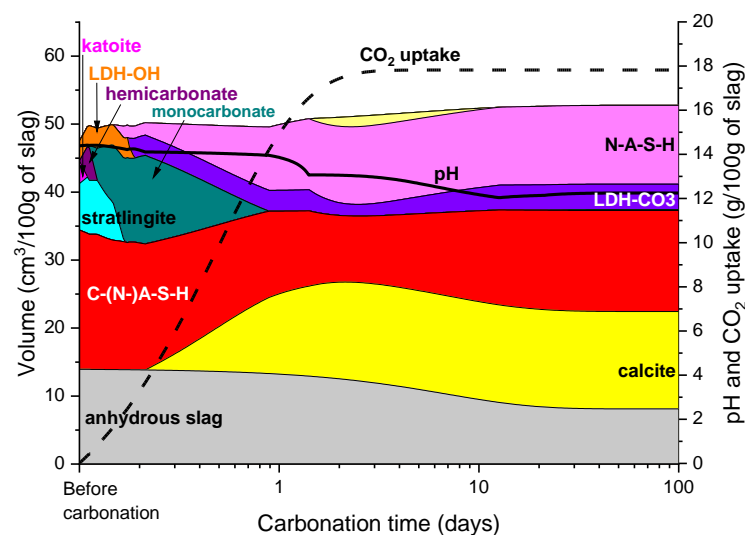
(b)

Figure 2. Simulated (a) phase assemblage and (b) chemical composition of C-(N-)A-S-H gel and LDH in the NaOH-activated slag sample as a function of carbonation time.

The calculations agree well with the experimental observations before carbonation as shown in Figure 3–Figure **6**. The dominant reaction products of the NaOH–activated slag reflected in the XRD pattern in Figure 3 are C-(N-)A-S-H and hydrotalcite-like phases (reflections similar to $Mg_2Al(OH)_6(CO_3)_{0.5} \cdot 1.5H_2O$, PDF 01-089-0460; hereafter LDH, see Fig. S1). TGA indicates the presence of C-(N-)A-S-H, with a broad mass loss at approximately 100 °C, and AFm phases such as strätlingite, hemicarbonate, and/or hydrotalcite, as evidenced by the shoulder at 180 °C [46, 47]. The ^{27}Al NMR spectrum of the NaOH–activated slag before carbonation in Figure **5** exhibits resonances at 74 and 9.5 ppm, due to the presence of the Al(IV) sites in C-(N-)A-S-H and Al(VI) in LDH [31]. The observed intensity at chemical shifts corresponding to q^3 sites can be attributed to cross-linking in C-(N-)A-S-H gels [31], while there is significant overlap with the remnant slag which gives a broad resonance spanning over the tetrahedral and pentahedral regions. The ^{29}Si MAS NMR spectra in Figure 6 confirm the presence of C-(N-)A-S-H with Q^1 and Q^2 silica sites, and the presence of strätlingite contributes to the resonance at approxmiately -85 ppm [48]. Note that all the spectra were normalized for

12

visualization of the decomposed sites, making the signal-to-noise ratio in the spectra of carbonated samples relatively larger than those with narrower peak shapes (uncarbonated sample). The MCL of C-(N-)A-S-H in the hydrated sample calculated using thermodynamic modeling and from the decomposed ^{29}Si MAS NMR spectra are 8.6 and 8.5, respectively, showing excellent agreement (Figure 7).
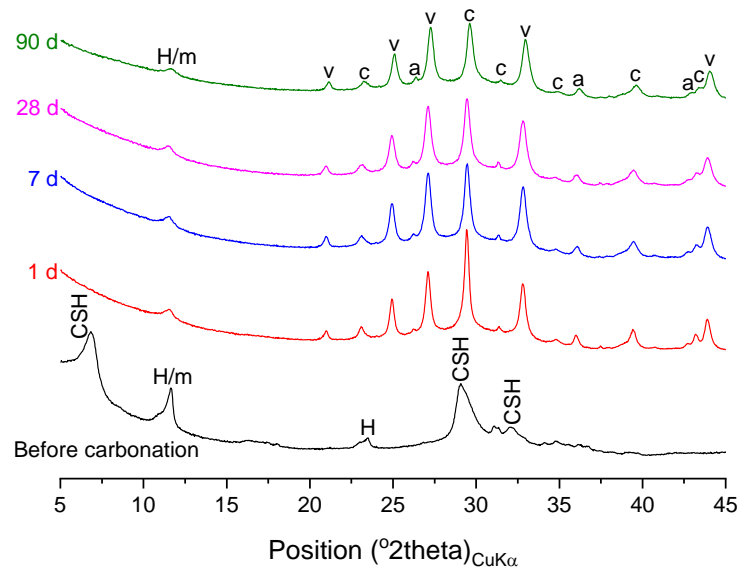

Figure 3. X-ray diffraction patterns for the NaOH-activated slag sample before carbonation, and after 1, 7, 28, and 90 d of carbonation. The annotations indicate the following: CSH- C-(N-)A-S-H, H- hydrotalcite, m- monocarbonate, a- aragonite, c- calcite and v- vaterite.
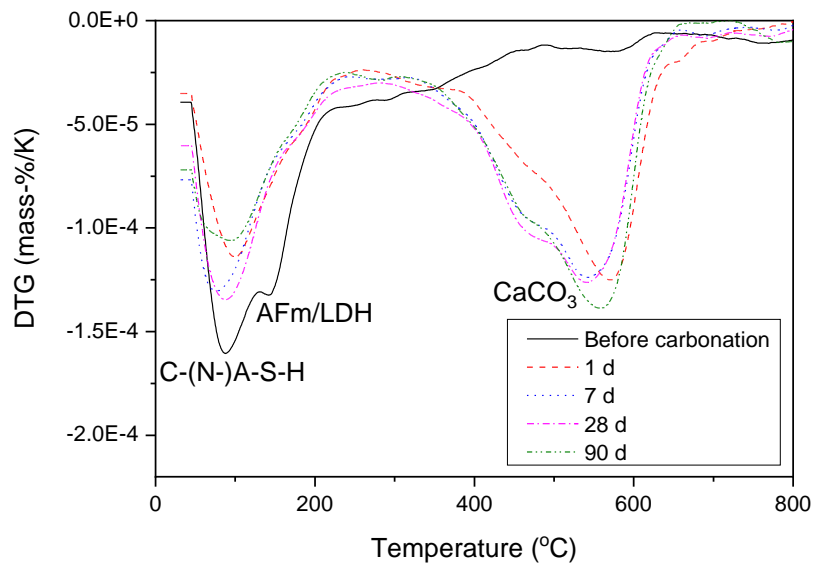
13

Figure 4. DTG of the NaOH-activated slag sample before carbonation, and after 1, 7, 28, and 90 d of carbonation.
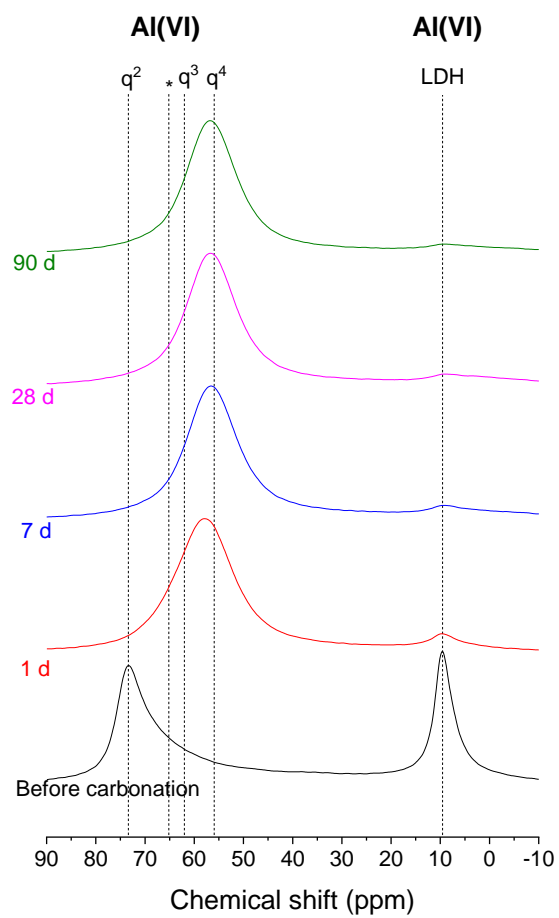
Figure 5. ^{27}Al MAS NMR spectra of the NaOH-activated slag sample before carbonation, and after 1, 7, 28, and 90 d of carbonation. The asterisk corresponds to the center of the resonance due to anhydrous slag.
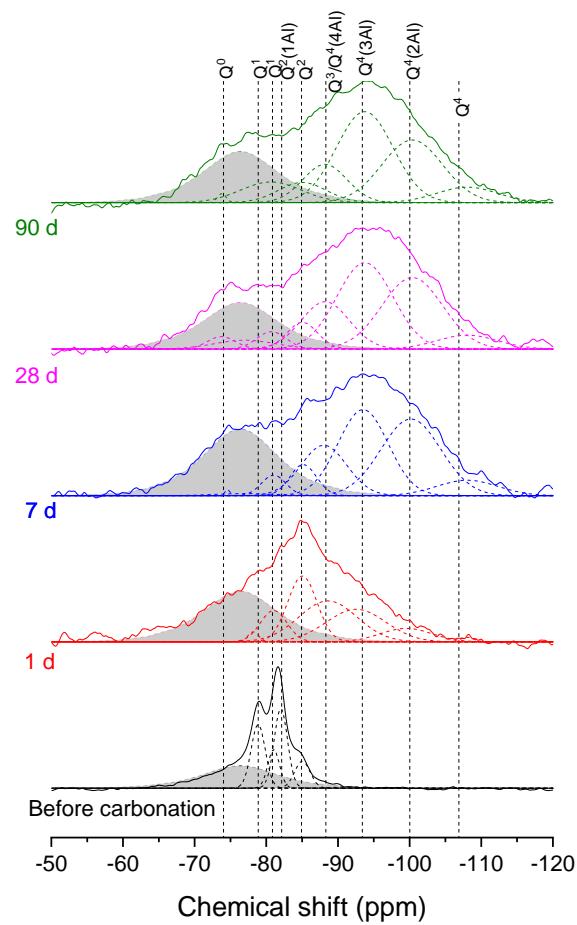
Figure 6. ^{29}Si MAS NMR spectra of the NaOH-activated slag sample before carbonation, and after 1, 7, 28, and 90 d of carbonation. The gray band represents the contribution of the anhydrous slag.
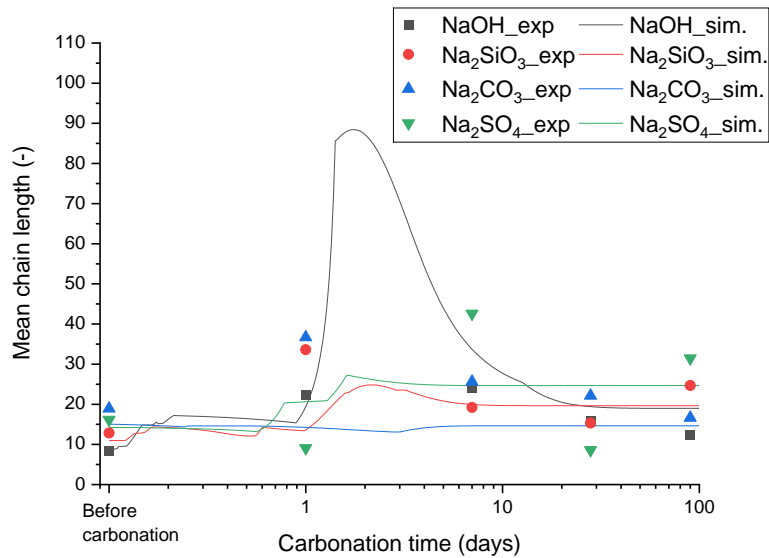
Figure 7. Mean chain length of alkali–activated slags calculated from the deconvolution of ^{29}Si MAS NMR spectra (dots) and thermodynamic modeling (lines).

The thermodynamic calculations predict upon carbonation the destabilization of katoite and hemicarbonate to monocarbonate and eventually to strätlingite, and CO_2 uptake by LDH. The Mg/Al ratio of OH-LDH gradually decreases upon carbonation until it reaches a ratio of ~2 (Figure 2 (b)). As carbonation proceeds, the formation of calcite is predicted, while C-(N-)A-S-H is expected to decalcify progressively; the Ca/Si ratio of C-(N-)A-S-H is predicted to decrease from 0.99 to ~0.89 (Figure 2 (b)) and N-A-S-H is predicted to form. The calculated Ca/Si ratio of C-(N-)A-S-H is expected to further decrease once all monocarbonates are converted to N-A-S-H gels. The calculated Na/Si ratio of C-(N-)A-S-H does not notably change upon carbonation, but the Ca/Si and Al/Si ratios drop when monocarbonate is depleted after 1 d of carbonation. The continuing reaction of the slag leads to the formation of additional N-A-S-H and C-(N-)A-S-H. The calculated pH value drops from 14.38 to 12.25 after 90 d of carbonation.

17

In agreement with the calculations presented above it was found experimentally that carbonation reduces the intensity of the monocarbonate/LDH and the C-(N-)A-S-H phase as illustrated in XRD, which implies that these phases are carbonated. The carbonation products identified by the XRD shown in Figure 3 are calcium carbonate polymorphs, predominantly calcite ($CaCO_3$, PDF 5-586) and vaterite ($CaCO_3$, PDF 33-628), and a minor quantity of aragonite ($CaCO_3$, PDF 01-073-3251). The obtained XRD patterns indicate no further changes in the hydrates after the 1st day of carbonation. The TGA results shown in Figure 4 support the XRD results, as the mass loss hump observed in the DTG curves upon decarbonation, which onsets at ~300 °C and offsets at 675 °C for a similar binder [10], notably increases during the 1st day of carbonation, and thereafter only a marginal increase is observed. The two mass loss humps observed between 300-700 °C after carbonation are both due to decarbonation, while the first hump is due to the presence of amorphous calcium carbonates and the second one is due to crystalline calcium carbonates [49, 50].

The ^{27}Al NMR spectra shows that the intensity of the resonances at the q^2 and Al(VI) sites decreases notably upon carbonation, and mostly converges to the new resonance being observed at 57–58 ppm, which is attributed to the presence of q^4 sites in N-A-S-H [28, 51]. Considering that the presence of LDH persists even after 90 d of carbonation as suggested by the XRD and the modeling results, the weak remaining resonance in the Al(VI) site, which is significantly lowered but is just above the background, can be assigned to LDH.

The presence of the q^4 sites in the carbonated NaOH-slag is supported by the ^{29}Si MAS NMR spectra shown in Figure 6, which show new resonances upon carbonation at -89, -93, -100 and -107 ppm which are assigned to the $Q^4(4Al)$, $Q^4(3Al)$, $Q^4(2Al)$ and $Q^4(1Al)$ sites, respectively [28]. The resonances at these sites reportedly arise from the presence of silica gels and/or N-A-S-H gels, as described in previous studies [28, 51], which form when C-(N-)A-S-H is carbonated. The dissolution of strätlingite and other AFm phases upon carbonation results in

the formation of N-A-S-H, which is already known to formed from the carbonation of C-(N-)A-S-H. The spectral deconvolution in Table 3 also shows a decrease in Al bound in C-(N-)A-S-H (less $Q^2(1Al)$) due to carbonation. The degree of reaction of the slag as quantified by the spectral deconvolution shown in Table 3 increases as the carbonation proceeds with a notable increase in the relative area of the sites assigned to N-A-S-H, in the Q^3–Q^4 but mainly the $Q^4(nAl)$ sites. In terms of Si and Al coordination, both the modeling and experimental results are in good agreement with each other.

Table 3. The relative area (%) of the sites obtained from the deconvolution of the ^{29}Si MAS NMR spectra of the NaOH-activated slag sample as a function of carbonation time.

Time (d)	Slag	Q^0	Q^1	Q^1	$Q^2(1Al)$	Q^2	$Q^3/$ $Q4(4Al)$	$Q^4(3Al)$	$Q^4(2Al)$	Q^4
	-	-74 ppm	-79 ppm	-81 ppm	-82 ppm	-85 ppm	-91 ppm	-93 ppm	-100 ppm	-107 ppm
0*	39	0	19	10	23	9	1	0	0	0
1	34	0	1	7	0	16	20	16	6	1
7	28	0	1	3	0	4	12	23	24	5
28	21	2	3	3	0	4	12	27	24	5
90	23	0	0	7	0	5	9	29	21	5

* Before carbonation

The thermodynamic modeling results shown in Figure 8 suggest that C-(N-)A-S-H, OH-LDH and strätlingite are initially present in the Na_2SiO_3-activated slag. The hydration and carbonation products of the Na_2SiO_3-activated slag share features that are similar to those observed in NaOH-activated slag. Specifically, C-(N-)A-S-H and hydrotalcite are identified as the reaction products in the XRD pattern (Figure 9), while strätlingite formation is not clearly observed in the Na_2SiO_3-activated slag, in contrast to the thermodynamic predictions. This could indicate that either the Al-uptake in C-(N-)A-S-H is underestimated in the model, and/or that the strätlingite present is poorly crystalline and thus not well visible by XRD. The ^{27}Al MAS NMR spectra of the Na_2SiO_3-activated samples as shown in Figure 11, however, indicate

the presence of some strätlingite (or other AFm phases as indicated by the signal at approximately 10 ppm). A notable difference in the Al(VI) environment is the intensity of the resonance at 4.5 ppm assigned to the third aluminate hydrate (TAH) [52, 53], which is higher in the spectrum of the Na_2SiO_3-activated slag than for the NaOH-activated slag. The resonance due to the q^2 aluminate species in C-(N-)A-S-H is observed at two different locations (74 and 68 ppm). The signal at 74 ppm is mainly attributed to the lower electron density, arising from the neighboring Q^1 Si sites connected to either H^+ or Na^+ in the bridging sites of C-(N-)A-S-H [31, 54]. The more notably intense resonance at 68 ppm in comparison to that in the NaOH-activated slag before carbonation therefore indicates a higher population of the q^2 aluminate species neighboring a Q^1 Si connected to Ca^{2+} in the Na_2SiO_3-activated slag, which is due to the lower amount of Na^+ ions added by the activator, and/or it may imply a higher amount of strätlingite [48]. The presence of C-(N-)A-S-H is also clearly visible in the Si-NMR data shown in Figure 12. The MCL of C-(N-)A-S-H in the hydrated sample calculated using the spectral deconvolution and the modeling is similar, showing values of 13 and 11 (Figure 7); thus, it is slightly higher than that present in the NaOH-activated slag, which is attributed to the SiO_2 added to the system by the activator, increasing the chain length [4, 55].
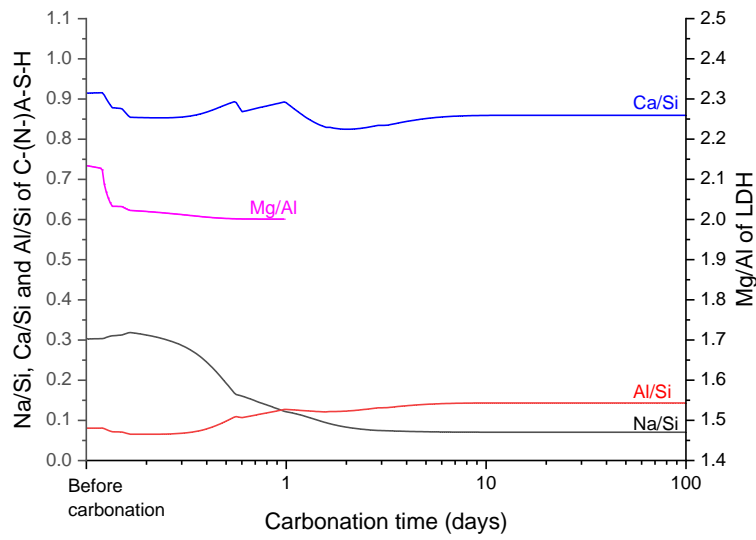
(a)
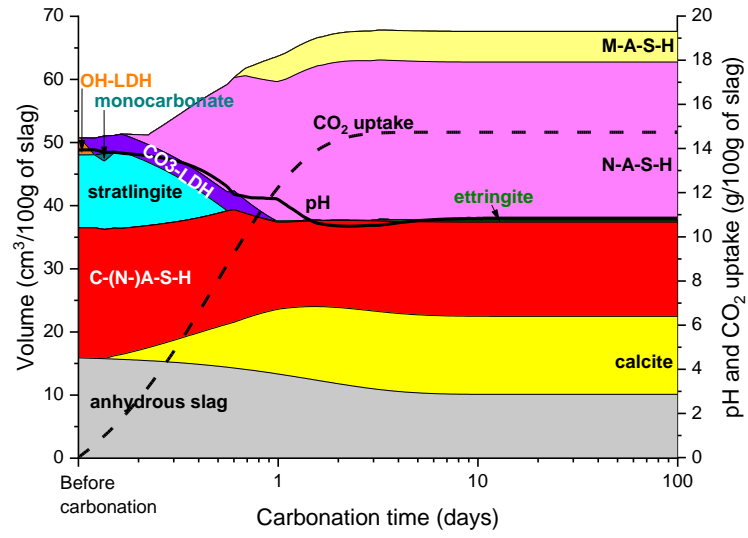
(b)

Figure 8. Simulated (a) phase assemblage and (b) chemical composition of C-(N-)A-S-H gel and LDH in the Na_2SiO_3-activated slag sample as a function of carbonation time.
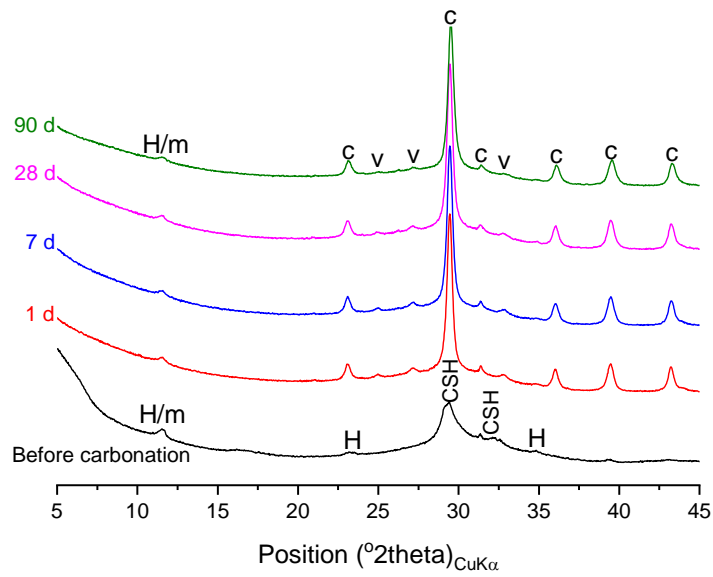
Figure 9. X-ray diffraction patterns for the Na$_2$SiO$_3$-activated slag sample before carbonation, and after 1, 7, 28, and 90 d of carbonation. The annotations indicate the following: CSH- C-(N-)A-S-H, H- hydrotalcite, m- monocarbonate, c- calcite and v- vaterite
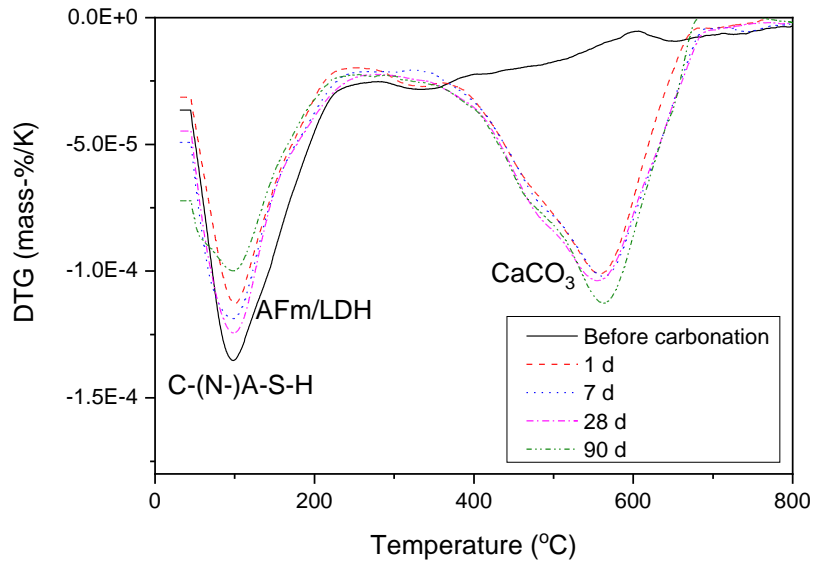

Figure 10. DTG of the Na$_2$SiO$_3$-activated slag sample before carbonation, and after 1, 7, 28, and 90 d of carbonation
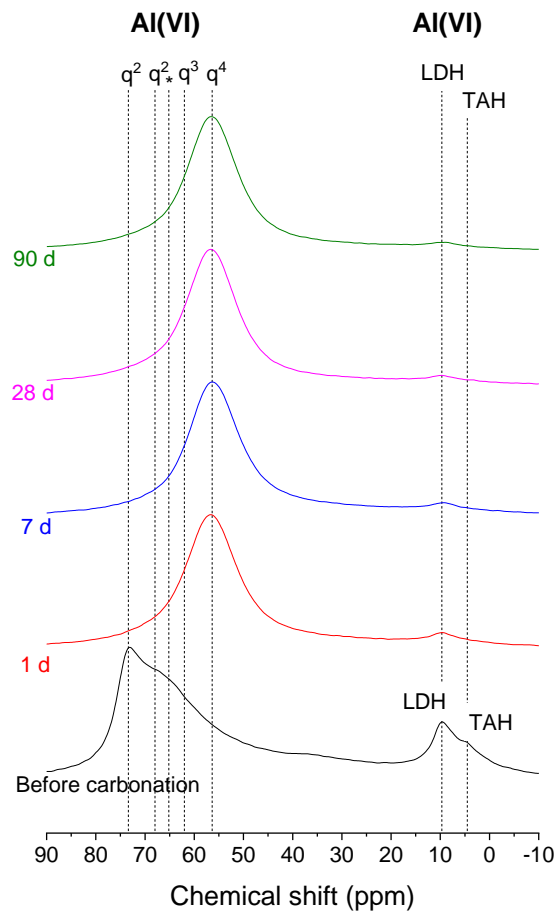
Figure 11. ^{27}Al MAS NMR spectra of the Na$_2$SiO$_3$-activated slag sample before carbonation, and after 1, 7, 28, and 90 d of carbonation. The asterisk corresponds to the center of the resonance due to anhydrous slag.
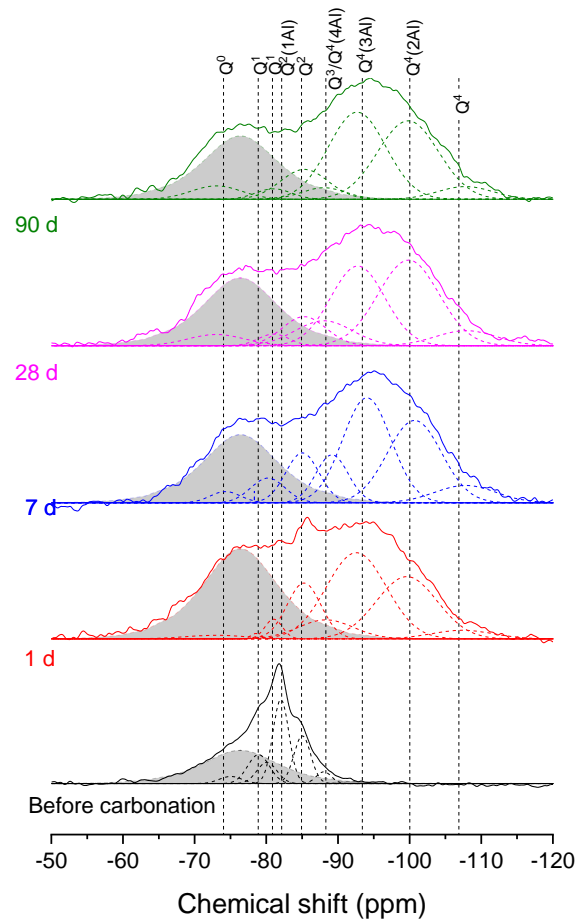
Figure 12. ^{29}Si MAS NMR spectra of the Na$_2$SiO$_3$-activated slag sample before carbonation, and after 1, 7, 28, and 90 d of carbonation. The gray band represents the contribution of the anhydrous slag.

The thermodynamic calculations in Figure 8 indicate that upon carbonation a minor quantity of monocarbonate forms as a transient phase at an early stage of carbonation. In addition, the CO$_2$ uptake by LDH is calculated to occur relatively early, prior to the destabilization of monocarbonate to strätlingite. Further carbonation is seen to decalcify C-(N-)A-S-H gel down to Ca/Si = 0.88 and then both strätlingite and C-(N-)A-S-H gel start destabilizing to N-A-S-H. The Na/Si ratio of the C-(N-)A-S-H gel starts decreasing at this point, which can be attributed to the stabilization of N-A-S-H, which binds Na, by carbonation. M-

24

A-S-H is predicted stable after ~0.6 d of carbonation. The thermodynamic preference of M-A-S-H over LDH in this system as compared to the NaOH-activated system can be attributed to the lower Na_2O concentrations, thus lower pH values, and the higher availability of SiO_2 provided by the activator, which stabilizes M-A-S-H over LDH, at a relatively early stage of carbonation. Nevertheless, it is difficult to experimentally confirm its formation, due to its disordered nature and significant overlap with the resonance of C-(N-)A-S-H and highly crosslinked aluminosilicate gels in ^{29}Si MAS NMR spectra. Formation of M-S-H (or M-A-S-H) in alkali-activated slag is experimentally found only when Mg^{2+} is externally provided (i.e., as an activator [56, 57] or due to exposure to Mg-containing environments such as seawater [58]). The simulated pH exhibits a notable drop, i.e., from 13.95 to 12.23 and to 11.69, respectively, after strätlingite and CO3-LDH are destabilized by carbonation.

The XRD patterns of the Na_2SiO_3-activated slag samples after carbonation mainly show reflections due to calcite with minor reflections due to vaterite, implying that the thermodynamically more stable calcium carbonates are predominantly formed in the Na_2SiO_3-activated slag by carbonation, thus showing less kinetic effects than the NaOH-activated slag system. Despite the mineralogical difference in the carbonation products formed in the Na_2SiO_3- and NaOH-activated slag samples, both samples exhibit a similar decarbonation behavior in the DTG curves, showing onset and offset temperatures at 310-350 °C and 660-680 °C, respectively (Figure 4 and Figure 10). The ^{27}Al NMR spectra of the carbonated Na_2SiO_3-activated slag can be resolved into two main sites, similar to the carbonated NaOH-activated slag; a predominant q^4 aluminate species after carbonation and a minor population of LDH, regardless of carbonation time. The formation of the q^4 aluminate species observed in the ^{27}Al MAS NMR spectra of the carbonated samples is associated with the formation of N-A-S-H, which also gives rise to the resonances at the $Q^4(nAl)$ Si sites in the ^{29}Si MAS NMR spectra (Figure 12). The reaction degree of the slag quantified in Table 4 sharply increases

during the first days of carbonation, after 7 d of carbonation little further difference is observed. In addition, the degree of carbonation quantified by the TGA is found to stop increasing after 28 and 90 d of carbonation, showing a decreased rate of carbonation as a function of time and reaction degree.

Table 4. The relative area (%) of the sites obtained from the deconvolution of the ^{29}Si MAS NMR spectra of the Na_2SiO_3-activated slag sample as a function of carbonation time.

Time (d)	Slag	Q^0	Q^1	Q^1	$Q^2(1Al)$	Q^2	$Q^3/$ $Q^4(4Al)$	$Q^4(3Al)$	$Q^4(2Al)$	Q^4
	-	-74 ppm	-79 ppm	-81 ppm	-82 ppm	-85 ppm	-91 ppm	-93 ppm	-100 ppm	-107 ppm
0*	43	3	10	7	21	13	3	1	0	0
1	36	1	0	2	0	9	5	25	19	3
7	27	2	0	4	0	8	8	25	22	5
28	27	3	3	2	0	6	7	21	26	5
90	28	4	0	2	0	8	3	27	26	4

* Before carbonation

The predicted phase assemblage of the Na_2CO_3-activated slag in Figure 13 shows that C-(N-)A-S-H, calcite, CO3-LDH and monocarbonate are present before carbonation. The reflections due to calcite, hemicarbonate ($Ca_4Al_2(OH)_{12}(OH)(CO_3)_{0.5} \cdot 5H_2O$, PDF 41-0221), monocarbonate ($Ca_4Al_2(OH)_{12}(CO_3) \cdot 5H_2O$, PDF 01-087-0493), hydrotalcite and gaylussite ($Na_2Ca(CO_3)_2 \cdot 5H_2O$, PDF 01-074-1235) are observed in the XRD pattern for the Na_2CO_3-activated slag (Figure 14). The DTG curve of the sample before carbonation in Figure 15 confirms the presence of C-(N-)A-S-H by the broad mass loss at approximately 100 °C [47]. The shoulder at 180°C and the broad mass loss hump at 300 °C in the sample before carbonation, is assigned to the dehydroxylation of the AFm and LDH phases [47]. The two q^2 aluminate species in the Al(IV) environment, as well as the TAH in the Al(VI) environments, observed in the ^{27}Al MAS NMR spectrum of the sample before carbonation (Figure 16) are attributed to the Al in C-(N-)A-S-H. The presence of the q^4 aluminate observed in the ^{27}Al MAS NMR spectrum and the $Q^3/Q^4(4Al)$ sites in the ^{29}Si MAS NMR spectrum of the uncarbonated sample in Figure 17

and Table 5 suggests that a minor quantity of N-A-S-H is possibly present before this sample is subjected to an elevated CO_2 condition. Specifically, this observation may be related to the presence of zeolite A ($Na_{12}Al_{12}Si_{12}O_{48} \cdot 18H_2O$) and/or Ca-heulandite ($CaAl_2Si_7O_{18} \cdot nH_2O$, $n=$ 3.5-6), although zeolites are transient phases only present in the early age of reaction, according to the previous study by Bernal et al. [18]. The MCL of the C-(N-)A-S-H gel in this sample calculated from the modeling and spectral deconvolution is 15 and 19, respectively, showing similar values, which are much higher than that of the other two samples discussed above.
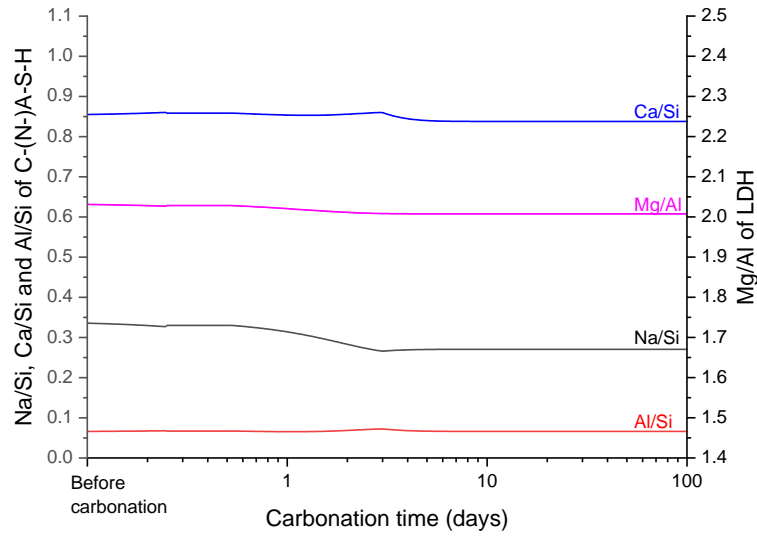
(a)

27
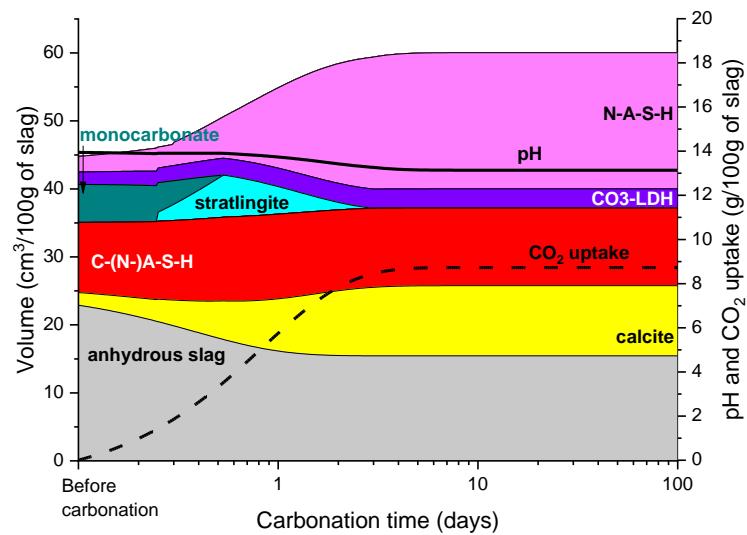
(b)

Figure 13. Simulated (a) phase assemblage and (b) chemical compositions of C-(N-)A-S-H gel and LDH in the Na_2CO_3-activated slag sample a function of carbonation time. The amount of CO_2 introduced by the activator has been excluded from the CO_2 uptake.
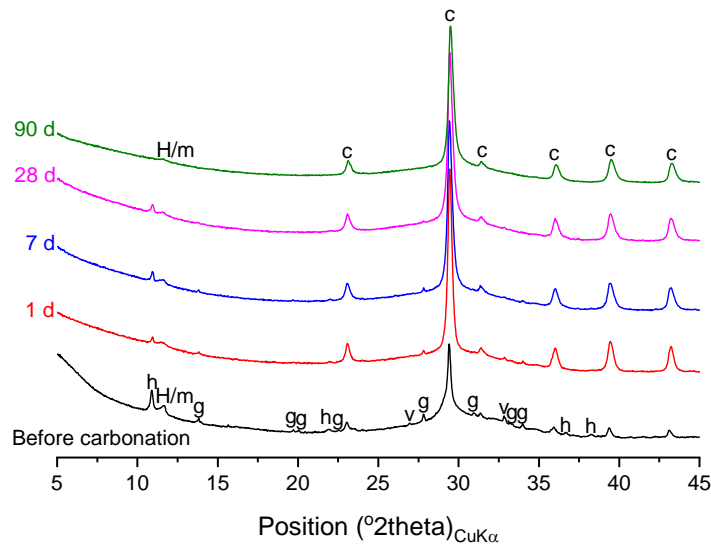

Figure 14. X-ray diffraction patterns for the Na_2CO_3-activated slag sample before carbonation, and after 1, 7, 28, and 90 d of carbonation. The annotations indicate the following: H- hydrotalcite, h- hemicarbonate, m- monocarbonate, g- gaylussite and c- calcite.
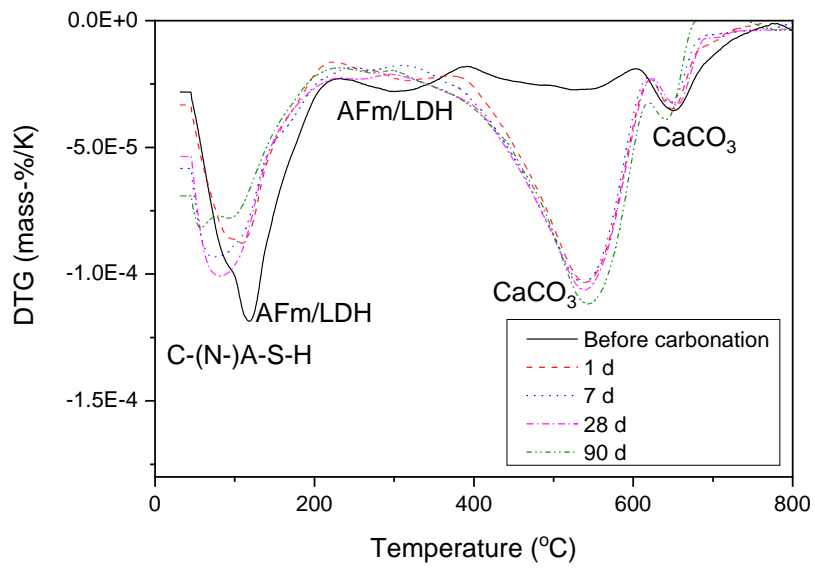
Figure 15. DTG of the Na$_2$CO$_3$-activated slag sample before carbonation, and after 1, 7, 28, and 90 d of carbonation.
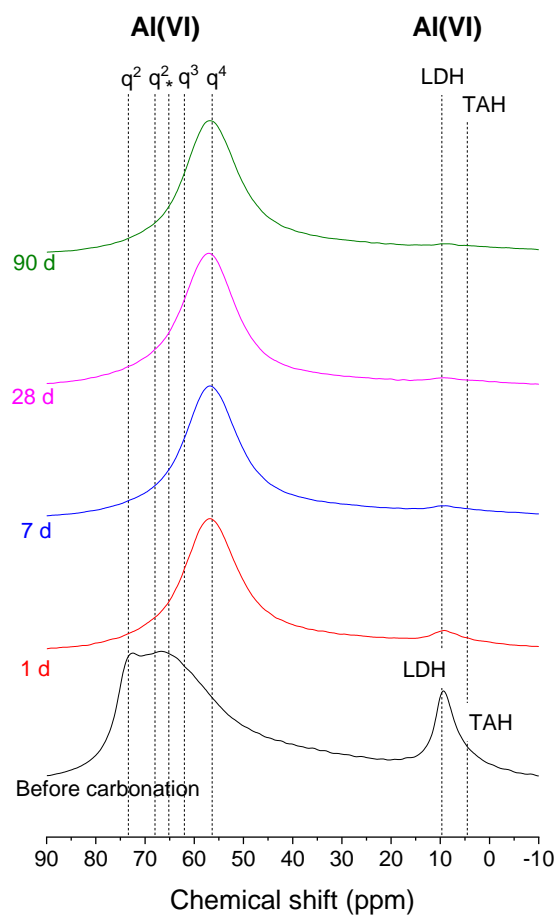
Figure 16. ^{27}Al MAS NMR spectra of the Na$_2$CO$_3$-activated slag sample before carbonation, and after 1, 7, 28, and 90 d of carbonation. The asterisk corresponds to the center of the resonance due to anhydrous slag.
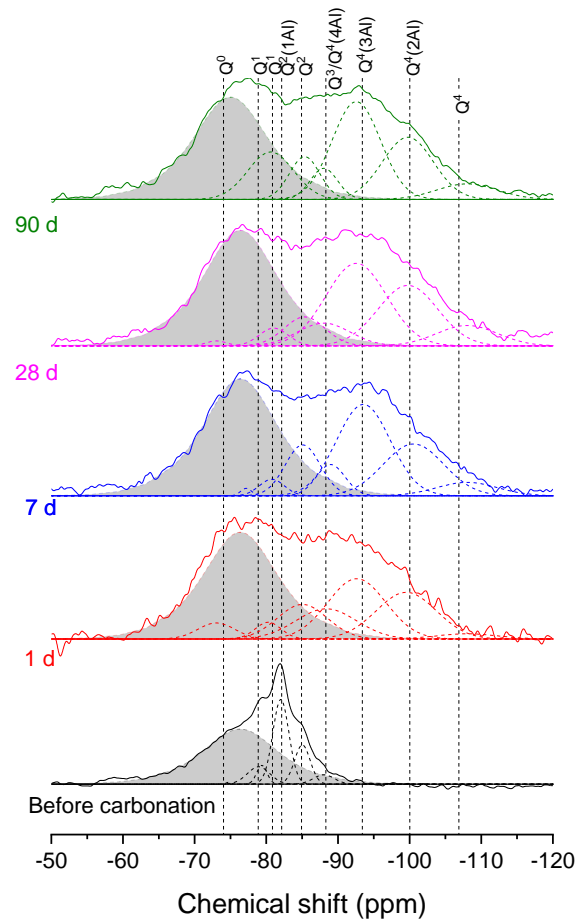
Figure 17. ^{29}Si MAS NMR spectra of the Na_2CO_3-activated slag sample before carbonation, and after 1, 7, 28, and 90 d of carbonation. The gray band represents the contribution of the anhydrous slag.

The simulations predict a destabilization of monocarbonate to strätlingite and ultimately to N-A-S-H. The simulated effect of carbonation on the gel chemistry is found to be less apparent, compared to the other two systems discussed above; the Na/Si, Ca/Si and Al/Si ratios of C-(N-)A-S-H changes from 0.33, 0.85 and 0.07 to 0.27, 0.84 and 0.07, respectively, and CO_3-LDH remains stable throughout the simulation with its Mg/Al unchanged at 2.0. This result may be attributed to the CO_2 incorporated by the activator, which leads to some extent

of carbonation to have proceeded before the samples are actually exposed to CO_2-rich atmosphere.

The reflections due to hemicarbonate and monocarbonate are also detected in the XRD pattern for the sample up to 28 d of carbonation. Similarly, the reflection of gaylussite is observed in the sample up to 7 d of carbonation, implying that these phases are transient and only stable during the corresponding carbonation time. The XRD pattern for the sample after 90 d of carbonation only presents the reflections due to calcite and LDH. Two humps are observed in the DTG curves of the carbonated samples at 540 and 650 ºC, which are attributed to the decarbonation of calcite, as identified in the XRD pattern. The disappearance of the shoulder at 120°C during carbonation indicates the destabilization of strätlingite [47], which is in good agreement with the thermodynamic modeling result. Similar to the other activator systems, carbonation leads to a substantial increase in the intensity of the resonances due to the q^4 aluminate in the ^{27}Al NMR spectra, while the intensity at other sites decrease because of the destabilization of C-(N-)A-S-H and other aluminate hydrates. Similarly, the intensity of the $Q^4(nAl)$ Si sites increases after carbonation (Table 5).

Table 5. The relative area (%) of the sites obtained from the deconvolution of the ^{29}Si MAS NMR spectra of the Na_2CO_3-activated slag sample as a function of carbonation time.

| Time (d)	Slag	Q^0	Q^1	Q^1	$Q^2(1Al)$	Q^2	$Q^3/$ $Q4(4Al)$	$Q^4(3Al)$	$Q^4(2Al)$	Q^4
	-	-74 ppm	-79 ppm	-81 ppm	-82 ppm	-85 ppm	-91 ppm	-93 ppm	-100 ppm	-107 ppm
0*	62	0	5	3	19	8	3	0	0	0
1	44	3	0	2	0	9	9	18	14	2
7	44	0	0	2	0	8	4	23	15	4
28	42	0	0	2	0	5	5	22	16	6
90	39	0	0	10	6	4	22	15	4	4

* Before carbonation

The predicted phase assemblage of the Na_2SO_4-activated slag in Figure 18 shows that C-(N-)A-S-H, N-A-S-H, ettringite, strätlingite and OH-LDH are present as reaction products. The main reaction products of the Na_2SO_4-activated slag identified in the XRD pattern in Figure 19 are ettringite ($Ca_6Al_2(SO_4)_3(OH)_{12} \cdot 26H_2O$, PDF 41-1451), and C-(N-)A-S-H, similar to the thermodynamic modeling result. The presence of ettringite as predicted by the modeling is supported by the DTG curve, which exhibits an intense mass loss at 100°C (Figure 20). Note that strätlingite was not experimentally observed in Na_2CO_3-[59] and Na_2SO_4-activated slag [60], while thermodynamic modeling results indicate that it is a stable phase in both systems [23, 61]. The ^{27}Al MAS NMR spectrum of the Na_2SO_4-activated slag sample before carbonation presented in Figure 21 shows the resonance at 13.5 ppm attributed to the presence of ettringite (marked as AFt in the Figure) [62, 63], and at 9.5 ppm attributed to the presence of LDH. The intensity of the resonance of the sites in the Al(IV) environment in the same spectrum is relatively weak, compared to other activator systems, which can be attributed to the notable formation of ettringite in this system; thus, Al is mostly associated with calcium aluminate hydrates, as opposed to the high population of Al observed in C-(N-)A-S-H in other activator systems.

The first carbonation product observed in the simulation is CO3-LDH. Strätlingite and CO3-LDH are expected to be destabilized to N-A-S-H and M-A-S-H, respectively, at a similar carbonation time. A minor quantity of sulfate-intercalated CO3-LDH is expected form at an early age of carbonation (Fig. S3 (d)). M-A-S-H is a carbonation product which is predicted stable in Na_2SiO_3- and Na_2SO_4-activated slag systems only. It can be attributed to the additional SiO_2 provided by the activator in the former case, and stability of ettringite and zeolites is preferred over MgAl-LDH upon carbonation, resulting in stabilizing M-A-S-H in the latter case. Upon depletion of CO3-LDH, ettringite partially dissolves and destabilizes to gypsum.

The initial pH of the pore solution in the Na_2SO_4-activated slag is predicted to be 13.45, and decrease to 13.03 when strätlingite is fully dissolved by carbonation. The pH further drops to 11.81 when CO3-LDH no longer buffers the carbonation, and reaches 10.94 at a later stage of carbonation. The Na/Si and Ca/Si ratios of C-(N-)A-S-H exhibit some changes over the course of carbonation, starting from 0.31 and 0.85 and reaching 0.21 and 0.79 at the end of the simulated carbonation time, respectively.
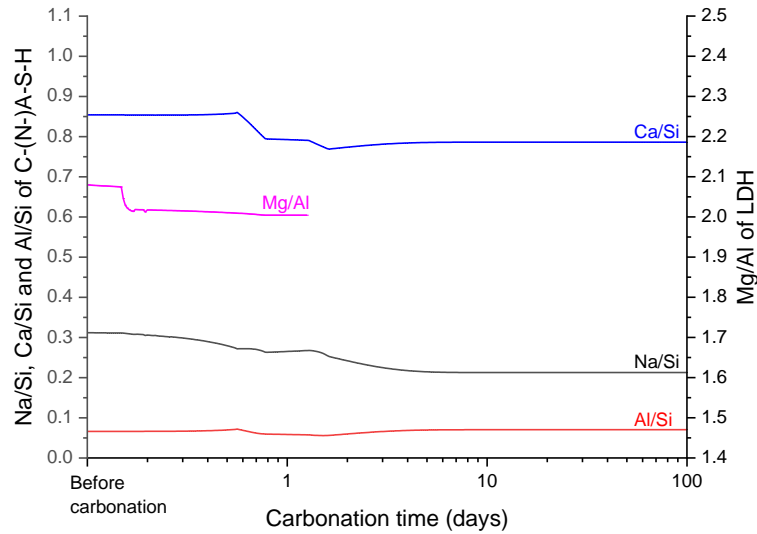
(a)
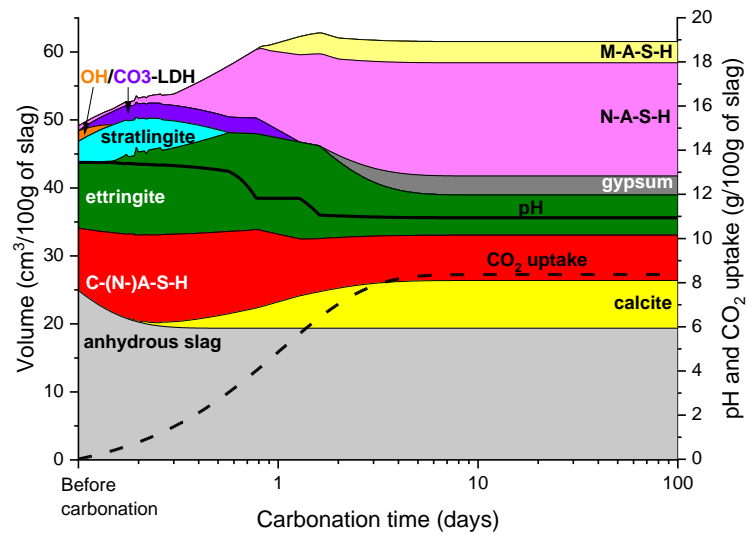
(b)

Figure 18. Simulated (a) phase assemblage and (b) chemical compositions of C-(N-)A-S-H gel and LDH in the Na_2SO_4-activated slag sample a function of carbonation time.

The amount of ettringite notably decreases after 1 d of carbonation in the XRD pattern, which also shows the reflections of vaterite and calcite as carbonation products. After 7 d of carbonation, the reflections due to ettringite are no longer observed, instead, bassanite ($CaSO_4 \cdot 0.5H_2O$, PDF 41-224) is found along with aragonite as a new carbonation product. The DTG curves of the carbonated samples exhibit two decarbonation humps centered at 510 °C and 635-660 °C with the latter one becoming stronger over carbonation time, and the curves show that carbonation progressively occurs in the samples over time.

The most notable difference between the thermodynamic calculation and the obtained experimental results is that gypsum ($CaSO_4 \cdot 2H_2O$) is predicted to form instead of bassanite ($CaSO_4 \cdot 0.5H_2O$), and ettringite is predicted to be stable even after 90 d of carbonation, which did not occur in the experiment. Such discrepancies are likely due to that fully saturated condition is considered in the simulation, which is unlikely to be met in the experimental

condition (60% R.H.), therefore affecting the stability of phases that exhibit high sensitivity to humidity such as ettringite and gypsum [64].

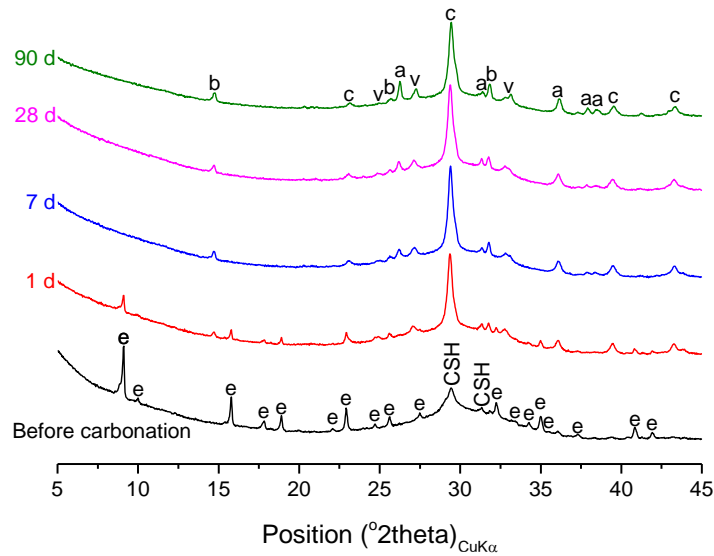

Figure 19. X-ray diffraction patterns for the Na_2SO_4-activated slag sample before carbonation, and after 1, 7, 28, and 90 d of carbonation. The annotations indicate the following: CSH- C-(N-)A-S-H, e- ettringite, b- bassanite, a- aragonite, v- vaterite and c- calcite.
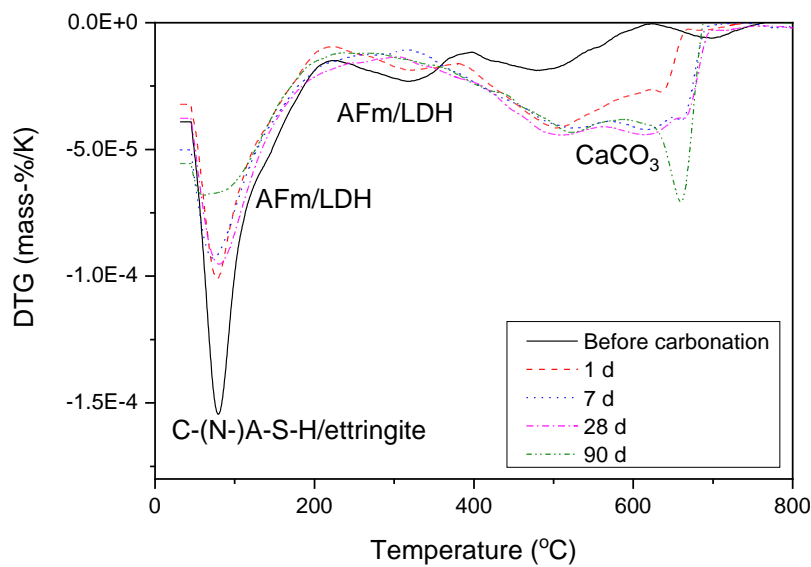

Figure 20. DTG of the Na_2SO_4-activated slag sample before carbonation, and after 1, 7, 28, and 90 d of carbonation.

The disappearance of ettringite after 1 and 7 d of carbonation is also observed in the NMR spectra, in good agreement with the XRD and TGA results. The resonance at 9.5 ppm attributed to the presence of LDH is persistently observed in the spectrum of the sample after 28 d of carbonation, suggesting that the stability of CO3-LDH may have been underestimated particularly for this activator system. The ^{29}Si MAS NMR spectra of the carbonated samples given in Figure 22 and the deconvolution summarized in Table 6 illustrate a significant increase in the Q^4(3Al) and Q^4(2Al) sites after carbonation, similar to the other activator systems. The carbonated samples generally have lower amounts of the residual slag, but they show no definite decreasing trend as a function of carbonation time after the first day, which might be related with the measurement error associated with the NMR technique and the spectral deconvolution process. This observation, together with the deconvolution results of other activator systems, which in fact yielded a clear decrease in the residual slag as a function of carbonation time, suggests that the dissolution of slag continues to some extent during carbonation.
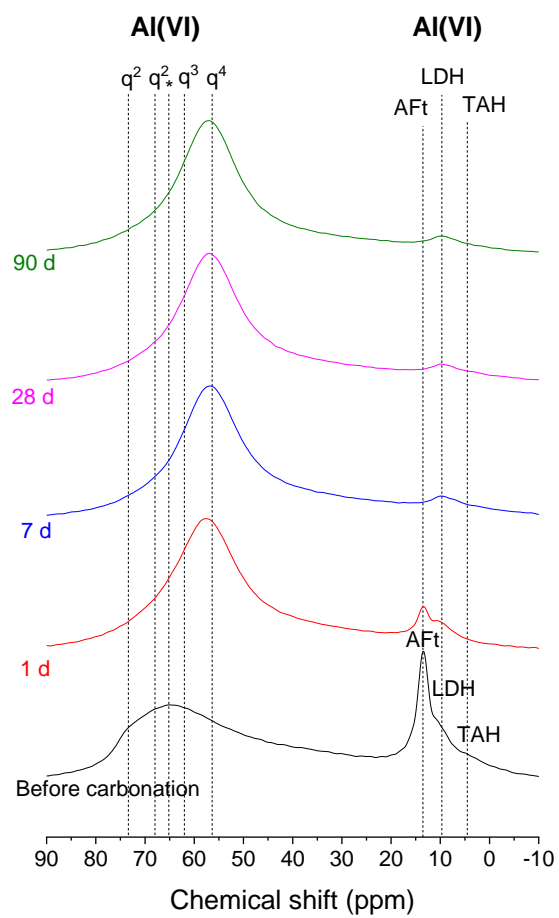
Figure 21. ^{27}Al MAS NMR spectra of the Na$_2$SO$_4$-activated slag sample before carbonation, and after 1, 7, 28, and 90 d of carbonation. The asterisk corresponds to the center of the resonance due to anhydrous slag.
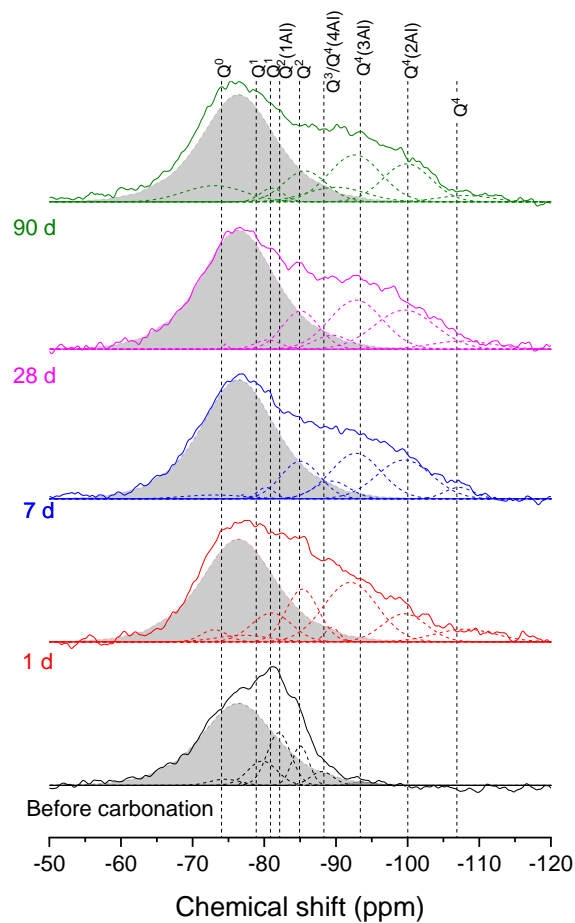
Figure 22. ^{29}Si MAS NMR spectra of the Na$_2$SO$_4$-activated slag sample before carbonation, and after 1, 7, 28, and 90 d of carbonation. The gray band represents the contribution of the anhydrous slag.

Table 6. The relative area (%) of the sites obtained from the deconvolution of the ^{29}Si MAS NMR spectra of the Na$_2$SO$_4$-activated slag sample as a function of carbonation time.

Time (d)	Slag	Q^0	Q^1	Q^1	Q^2(1Al)	Q^2	Q^3/ $Q4$(4Al)	Q^4(3Al)	Q^4(2Al)	Q^4
	-	-74 ppm	-79 ppm	-81 ppm	-82 ppm	-85 ppm	-91 ppm	-93 ppm	-100 ppm	-107 ppm
0*	67	2	0	7	13	7	3	1	0	0
1	48	2	2	7	0	10	1	18	7	4
7	57	1	0	1	0	9	4	13	13	2
28	52	0	7	1	0	7	3	14	13	3
90	52	6	0	2	0	8	5	15	11	2

* Before carbonation

Discussion

39

The MCL calculated from thermodynamic modeling and the deconvolution of the ^{29}Si MAS NMR spectra are compared in Figure 7. The values for the hydrated samples before carbonation calculated from both techniques are in an excellent agreement. Both techniques indicate an increase of MCL due to the decalcification of C-(N-)A-S-H during carbonation, but a significant variation in the obtained values occurs. The errors associated with these results from NMR data are relatively high due to the overlap of the resonance of C-(N-)A-S-H with strätlingite present in the hydrated slags and with the N-A-S-H gel that formed during carbonation. This also affects the accuracy of the obtained slag reaction degree, and thus the simulation results. The occurrence of an aluminosilicate gel instead of the predicted zeolite X further lowers the accuracy of the modeling. Therefore, the results of both techniques are bound to have a larger error margin for the carbonated cases. This is particularly noticeable in the calculated hump in the MCL of C-(N-)A-S-H in the NaOH-activated slag during 1st-10th d of carbonation, which may be associated with either underestimated slag reaction degree or overestimated CO_2 uptake at the corresponding carbonation time, making the model temporarily predict excessively decalcified C-(N-)A-S-H. Both techniques, however, clearly present that the MCL of C-(N-)A-S-H in alkali-activated slag tend to increase during carbonation in agreement with observations in previous studies [10, 51] where increases in Q^2 and Q^3, and Q^3/Q^4(2Al) Si, respectively, were shown in the ^{29}Si MAS NMR spectra of alkali–activated slag upon carbonation.

The CO_2 uptake of the samples per mass of hydrated slag in Figure 23 suggests that the NaOH-activated slag has the highest CO_2 binding capacity of 23.3 g per 100 g of hydrated slag (1 to 91 d), followed by that activated with Na_2SiO_3 (20.0 g/100g), Na_2SO_4 (15.8 g/100g) and Na_2CO_3 (13.8 g/100g). If the uptake of CO_2 added by the activator is also considered, the Na_2CO_3-activated slag takes up 21.0 g/100g, which is slightly higher than that of Na_2SiO_3, although the degree of slag reaction of the Na_2CO_3-activated slag is 55% lower than the 70%

reaction degree of the NaOH- and Na_2SiO_3-activated slags. If the CO_2 binding capacity at equal degree of slag reaction is compared, then the Na_2CO_3-activated slag has the highest CO_2 binding capacity, as shown in [65]. The higher standard error associated with the CO_2 uptake by the Na_2CO_3- and Na_2SO_4-activated samples is due to the much lower values observed on the first day of carbonation.

In addition to the CO_2 binding capacity, the pH of the pore solution has significant effect on the performance of the binders against steel corrosion. The pH of the simulated pore solution in the NaOH and Na_2CO_3 activated samples is calculated to remain above 12 and 13, respectively, while the pH within the other two samples is predicted to drop to 10-11 during carbonation (Figure 24). The calculated pH values for the samples after 90 d of carbonation is 12.3, 10.9, 13.1 and 10.9 for the NaOH-, Na_2SiO_3-, Na_2CO_3- and Na_2SO_4-activated samples, respectively. Note that a study by Ke et al. [65] showed that the pH is expected to drop to below 9 in all the systems upon complete carbonation. In the present study, high pH values are calculated by the modeling for these activators, which also showed a high CO_2 uptake per g of hydrated slag. As ground hydrated slag has been used in the experiments, the findings imply that the role of an alkali–activator in retaining the alkalinity in the pore solution during carbonation is not limited to affecting the matrix and CO_2 permeability. The activator seems to play an important role by inducing the development of a hydration phase assemblage that is more resistant to neutralization. For instance, SiO_2 added by the activator may stabilize M-A-S-H and destabilize MgAl-LDH, which buffers the pH of the pore solution. On the other hand, the activator dosages were identically applied on a mass basis (10g of each); thus, the Na_2O/slag mass ratios were different across the samples. The NaOH-activated system had the highest Na_2O dosage, which may have affected its pH evolution, CO_2 buffering capacity and overall carbonation behavior. It is however important to experimentally confirm whether these values are observed in the actual pore solution of the system and induce steel corrosion.

The thermodynamic modeling results predict that there is a volumetric increase for all activators during carbonation. This is in agreement with a study by Ke et al. [10], who reported a decrease in the mercury intrusion accessible porosity in Na_2CO_3 activated slag after carbonation. It is therefore possible that carbonation and $CaCO_3$ precipitation together with the additional slag reaction during carbonation lead to a decrease in the pore volume of alkali–activated slag and thus to an increase in solid volume. Although carbonation in alkali–activated slags is often observed to decrease their strength [29, 66], the opposite was observed in a previous study where Na_2CO_3 was used as an activator [10].
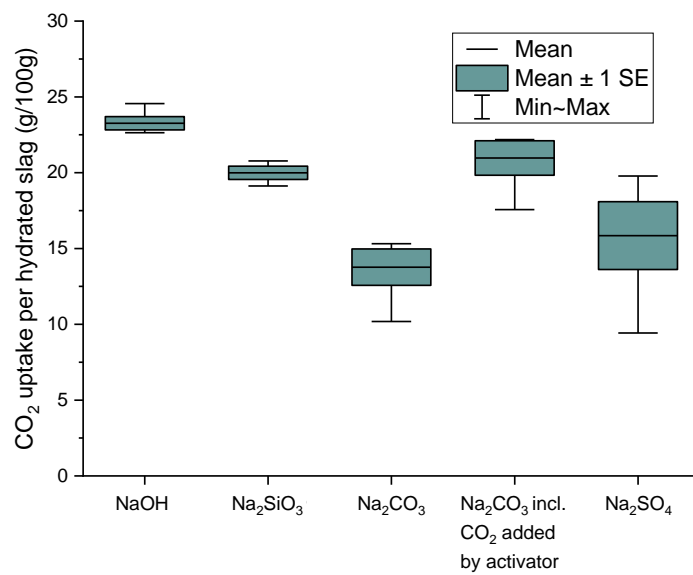

Figure 23. CO_2 uptake by alkali-activated slags per mass of hydrated slag between 1 to 90 d.
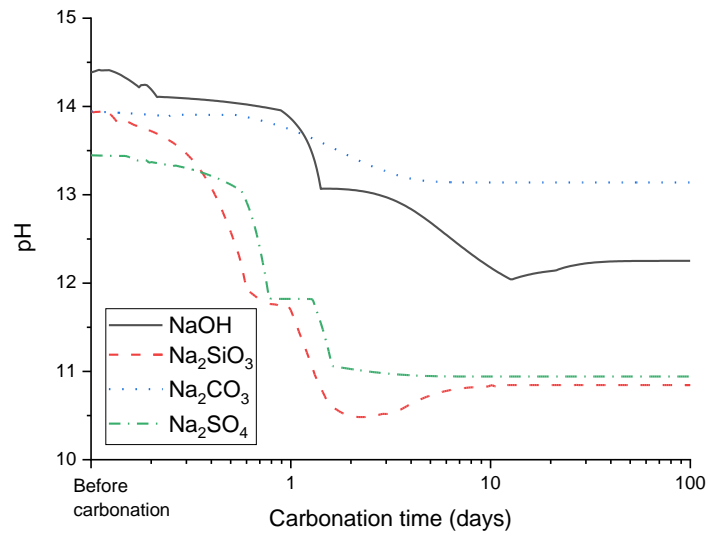
Figure 24. Simulated pH evolution in alkali–activated slags during carbonation.

Conclusions

The present study investigates the effect of carbonation on alkali–activated slag cements produced using various alkali–activators such as NaOH, Na_2SiO_3, Na_2CO_3 and Na_2SO_4. The following conclusions can be drawn from the thermodynamic modeling and experimental results obtained from the samples carbonated at 1% CO_2 concentration for up to 90 d:

(1) The main hydrates in NaOH- and Na_2SiO_3-activated slags were C-(N-)A-S-H, strätlingite and MgAl-layered double hydroxide phases. In the presence of Na_2CO_3 calcite and monocarbonate instead of strätlingite were present, while ettringite was observed in the Na_2SO_4 activated slag.

(2) In the NaOH- and Na_2SiO_3-activated slags a slag reaction of >70% was observed after carbonation, while a lower degree of slag reaction was observed for Na_2CO_3- (60%) and Na_2SO_4-activated (50%) slags. The carbonation of the pre-hydrated samples led to a renewed reaction of the slag, in particular in the case of the Na_2SO_4- and Na_2CO_3- activated slags, where the reaction degree was increased by ~1/3 during carbonation.

(3) The main carbonation products include calcium carbonate, CO_3-MgAl-layered double hydroxide and an aluminosilicate gel. In Na_2SiO_3- and Na_2SO_4-activated slags the destabilization of the MgAl-layered double hydroxide phases to M-S-H occurred. Carbonation also destabilized AFm phases such as strätlingite, hemicarbonate, and monocarbonate to an aluminosilicate gel.

(4) Although C-(N-)A-S-H was decalcified and its amount notably decreased after carbonation, C-(N-)A-S-H was not completely destabilized.

(5) AFm phases (including strätlingite) were easily degraded to calcium carbonate and

other solids by carbonation, while MgAl-LDH phases converted to carbonate-containing MgAl-LDH, which were more resistant to further carbonation degradation as experimentally observed and calculated using thermodynamic modeling.

(6) The CO_2 uptakes per mass of hydrated slag for the samples activated with NaOH, Na_2CO_3, Na_2SiO_3 and Na_2SO_4 were 23.3, 21.0, 20.0, and 15.8 g per 100 g, respectively, suggesting that the CO_2 binding capacity can be activator-dependent.

Supporting information

Additional XRD plots for showing hydrotalcite and monocarbonate, and decomposed NMR spectra

Acknowledgments

Conflict of interest

There is no conflict of interest to be declared.

Data availability

The raw/processed data that support the findings of this study are available from the corresponding author upon request.

References

1.   Gartner, E.; Hirao, H., A review of alternative approaches to the reduction of CO_2 emissions associated with the manufacture of the binder phase in concrete. *Cem. Concr. Res.* **2015,** *78*, 126-142, DOI: 10.1016/j.cemconres.2015.04.012

2.   Gartner, E.; Sui, T., Alternative cement clinkers. *Cem. Concr. Res.* **2018,** *114*, 27-39, DOI: 10.1016/j.cemconres.2017.02.002

3.   Shi, C.; Jiménez, A. F.; Palomo, A., New cements for the 21st century: The pursuit of an alternative to Portland cement. *Cem. Concr. Res.* **2011,** *41* (7), 750-763, DOI: 10.1016/j.cemconres.2011.03.016

4.   Wang, S.-D.; Scrivener, K. L., Hydration products of alkali activated slag cement. *Cem. Concr. Res.* **1995,** *25* (3), 561-571, DOI: 10.1016/0008-8846(95)00045-E

5.   Criado, M.; Walkley, B.; Ke, X.; Provis, J.; Bernal, S., Slag and Activator Chemistry Control the Reaction Kinetics of Sodium Metasilicate-Activated Slag Cements. *Sustainability* **2018,** *10* (12), 4709, DOI: 10.3390/su10124709

6.   Provis, J. L., Alkali-activated materials. *Cem. Concr. Res.* **2018,** *114*, 40-48, DOI: 10.1016/j.cemconres.2017.02.009

7.   Liu, J.; Wang, D., Influence of steel slag-silica fume composite mineral admixture on the properties of concrete. *Powder Technol.* **2017,** *320*, 230-238, DOI: 10.1016/j.powtec.2017.07.052

8.   Naidu, T. S.; Sheridan, C. M.; van Dyk, L. D., Basic oxygen furnace slag: Review of current and potential uses. *Miner. Eng.* **2020,** *149*, 106234, DOI: 10.1016/j.mineng.2020.106234

9.   Snellings, R., Assessing, understanding and unlocking supplementary cementitious materials. *RILEM Technical Letters* **2016,** *1*, 50-55, DOI: 10.21809/rilemtechlett.2016.12

10.   Ke, X.; Criado, M.; Provis, J. L.; Bernal, S. A., Slag-based cements that resist damage induced by carbon dioxide. *ACS Sustainable Chemistry & Engineering* **2018,** *6* (4), 5067-5075, DOI: 10.1021/acssuschemeng.7b04730

11.   Borba Jr, J. C.; Brigolini, G. J.; Oliveira, V. A.; Calmon, J. L.; Mariano, E. F., Steel Slag as a Precursor Material for Alkali-Activated Binders: A Systematic Review. **2022**, DOI: 10.20944/preprints202210.0137.v1

12.   Jiang, D.; Shi, C.; Zhang, Z., Recent progress in understanding setting and hardening of alkali-activated slag (AAS) materials. *Cem. Concr. Compos.* **2022**, 104795, DOI: 10.1016/j.cemconcomp.2022.104795

13.   Myers, R. J.; Lothenbach, B.; Bernal, S. A.; Provis, J. L., Thermodynamic modelling of alkali-activated slag cements. *Appl. Geochem.* **2015,** *61*, 233-247, DOI: 10.1016/j.apgeochem.2015.06.006

14.   Haha, M. B.; Le Saout, G.; Winnefeld, F.; Lothenbach, B., Influence of activator type on hydration kinetics, hydrate assemblage and microstructural development of alkali activated blast-furnace slags. *Cem. Concr. Res.* **2011,** *41* (3), 301-310, DOI: 10.1016/j.cemconres.2010.11.016

15.   Haha, M. B.; Lothenbach, B.; Le Saout, G.; Winnefeld, F., Influence of slag chemistry on the hydration of alkali-activated blast-furnace slag—Part I: Effect of MgO. *Cem. Concr. Res.* **2011,** *41* (9), 955-963, DOI: 10.1016/j.cemconres.2011.05.002

16.   Zuo, Y., Thermodynamic modeling of the phase evolution in alkali-activated slag

cements with sulfate salt exposure. *J. Am. Ceram. Soc.* **2022,** *105* (12), 7658-7675, DOI: 10.1111/jace.18661

17.   Ren, J.; Sun, H.; Li, Q.; Li, Z.; Zhang, X.; Wang, Y.; Li, L.; Xing, F., A comparison between alkali-activated slag/fly ash binders prepared with natural seawater and deionized water. *J. Am. Ceram. Soc.* **2022**, DOI: 10.1111/jace.18515

18.   Bernal, S. A.; Provis, J. L.; Myers, R. J.; San Nicolas, R.; van Deventer, J. S., Role of carbonates in the chemical evolution of sodium carbonate-activated slag binders. *Mater. Struct.* **2015,** *48* (3), 517-529, DOI: 10.1617/s11527-014-0412-6

19.   Mobasher, N.; Bernal, S. A.; Provis, J. L., Structural evolution of an alkali sulfate activated slag cement. *J. Nucl. Mater.* **2016,** *468*, 97-104, DOI: 10.1016/j.jnucmat.2015.11.016

20.   Prabahar, J.; Vafaei, B.; Baffoe, E.; Ghahremaninezhad, A., The effect of biochar on the properties of alkali-activated slag pastes. *Construction Materials* **2022,** *2* (1), 1-14, DOI: 10.3390/constrmater2010001

21.   Vafaei, B.; Farzanian, K.; Ghahremaninezhad, A., The influence of superabsorbent polymer on the properties of alkali-activated slag pastes. *Constr. Build. Mater.* **2020,** *236*, 117525, DOI: 10.1016/j.conbuildmat.2019.117525

22.   Abhishek, H.; Prashant, S.; Kamath, M. V.; Kumar, M., Fresh mechanical and durability properties of alkali-activated fly ash-slag concrete: a review. *Innovative Infrastructure Solutions* **2022,** *7* (1), 1-14, DOI: 10.1007/s41062-021-00711-w

23.   Myers, R. J.; Bernal, S. A.; Provis, J. L., Phase diagrams for alkali-activated slag binders. *Cem. Concr. Res.* **2017,** *95*, 30-38, DOI: 10.1016/j.cemconres.2017.02.006

24.   Bernal, S. A.; Provis, J. L., Durability of Alkali-Activated Materials: Progress and Perspectives. *J. Am. Ceram. Soc.* **2014,** *97* (4), 997-1008, DOI: 10.1111/jace.12831

25.   Wang, S.-D.; Pu, X.-C.; Scrivener, K.; Pratt, P., Alkali-activated slag cement and concrete: a review of properties and problems. *Adv. Cem. Res.* **1995,** *7* (27), 93-102, DOI:

10.1680/adcr.1995.7.27.93

26.   Kim, G.; Jang, J.; Naeem, F.; Lee, H., Heavy Metal Leaching, CO2 Uptake and Mechanical Characteristics of Carbonated Porous Concrete with Alkali-Activated Slag and Bottom Ash. *International Journal of Concrete Structures and Materials* **2015,** *9* (3), 283-294, DOI: 10.1007/s40069-015-0111-x

27.   Puertas, F.; Fernández-Jiménez, A.; Blanco-Varela, M. T., Pore solution in alkali-activated slag cement pastes. Relation to the composition and structure of calcium silicate hydrate. *Cem. Concr. Res.* **2004,** *34* (1), 139-148, DOI: 10.1016/S0008-8846(03)00254-0

28.   Bernal, S. A.; Provis, J. L.; Walkley, B.; San Nicolas, R.; Gehman, J. D.; Brice, D. G.; Kilcullen, A. R.; Duxson, P.; van Deventer, J. S., Gel nanostructure in alkali-activated binders based on slag and fly ash, and effects of accelerated carbonation. *Cem. Concr. Res.* **2013,** *53*, 127-144, DOI: 10.1016/j.cemconres.2013.06.007

29.   Shi, Z.; Shi, C.; Wan, S.; Li, N.; Zhang, Z., Effect of alkali dosage and silicate modulus on carbonation of alkali-activated slag mortars. *Cem. Concr. Res.* **2018,** *113*, 55-64, DOI: 10.1016/j.cemconres.2018.07.005

30.   Bernal, S. A.; Provis, J. L.; Brice, D. G.; Kilcullen, A.; Duxson, P.; van Deventer, J. S., Accelerated carbonation testing of alkali-activated binders significantly underestimates service life: the role of pore solution chemistry. *Cem. Concr. Res.* **2012,** *42* (10), 1317-1326, DOI: 10.1016/j.cemconres.2012.07.002

31.   Myers, R. J.; Bernal, S. A.; Gehman, J. D.; Deventer, J. S.; Provis, J. L., The Role of Al in Cross-Linking of Alkali-Activated Slag Cements. *J. Am. Ceram. Soc.* **2015,** *98* (3), 996-1004, DOI: 10.1111/jace.13360

32.   Park, S.; Jang, J.; Lee, H., Unlocking the role of MgO in the carbonation of alkali-activated slag cement. *Inorganic Chemistry Frontiers* **2018,** *5* (7), 1661-1670, DOI: 10.1039/C7QI00754J

33.   Sevelsted, T. F.; Skibsted, J., Carbonation of C–S–H and C–A–S–H samples studied by 13 C, 27 Al and 29 Si MAS NMR spectroscopy. *Cem. Concr. Res.* **2015,** *71*, 56-65, DOI: 10.1016/j.cemconres.2015.01.019

34.   Myers, R. J.; Bernal, S. A.; San Nicolas, R.; Provis, J. L., Generalized structural description of calcium–sodium aluminosilicate hydrate gels: the cross-linked substituted tobermorite model. *Langmuir* **2013,** *29* (17), 5294-5306, DOI: 10.1021/la4000473

35.   Kulik, D. A.; Wagner, T.; Dmytrieva, S. V.; Kosakowski, G.; Hingerl, F. F.; Chudnenko, K. V.; Berner, U. R., GEM-Selektor geochemical modeling package: revised algorithm and GEMS3K numerical kernel for coupled simulation codes. *Comput. Geosci.* **2013,** *17* (1), 1-24, DOI: 10.1007/s10596-012-9310-6

36.   Wagner, T.; Kulik, D. A.; Hingerl, F. F.; Dmytrieva, S. V., GEM-Selektor geochemical modeling package: TSolMod library and data interface for multicomponent phase models. *Can. Mineral.* **2012,** *50* (5), 1173-1195, DOI: 10.3749/canmin.50.5.1173

37.   Lothenbach, B.; Kulik, D. A.; Matschei, T.; Balonis, M.; Baquerizo, L.; Dilnesa, B.; Miron, G. D.; Myers, R. J., Cemdata18: A chemical thermodynamic database for hydrated Portland cements and alkali-activated materials. *Cem. Concr. Res.* **2019,** *115*, 472-506, DOI: 10.1016/j.cemconres.2018.04.018

38.   Gomez-Zamorano, L.; Balonis, M.; Erdemli, B.; Neithalath, N.; Sant, G., C–(n)–s–h and n–a–s–h gels: Compositions and solubility data at 25 c and 50 c. *J. Am. Ceram. Soc.* **2017,** *100* (6), 2700-2711, DOI: 10.1111/jace.14715

39.   Bernard, E.; Lothenbach, B.; Cau-Dit-Coumes, C.; Pochard, I.; Rentsch, D., Aluminum incorporation into magnesium silicate hydrate (MSH). *Cem. Concr. Res.* **2020,** *128*, 105931, DOI: 10.1016/j.cemconres.2019.105931

40.   Monnin, C.; Schott, J., Determination of the solubility products of sodium carbonate minerals and an application to trona deposition in Lake Magadi (Kenya). *Geochim. Cosmochim.*

Acta **1984,** *48* (3), 571-581, DOI: 10.1016/0016-7037(84)90285-0

41.   Königsberger, E.;   Königsberger, L.-C.; Gamsjäger, H., Low-temperature thermodynamic model for the system Na2CO3− MgCO3− CaCO3− H2O. *Geochim. Cosmochim. Acta* **1999,** *63* (19-20), 3105-3119, DOI: 10.1016/S0016-7037(99)00238-0

42.   Bernard, E.; Zucha, W. J.; Lothenbach, B.; Mäder, U., Stability of hydrotalcite (Mg-Al layered double hydroxide) in presence of different anions. *Cem. Concr. Res.* **2022,** *152*, 106674, DOI: 10.1016/j.cemconres.2021.106674

43.   Helgeson, H. C.;   Kirkham, D. H.; Flowers, G. C., Theoretical prediction of the thermodynamic behavior of aqueous electrolytes by high pressures and temperatures; IV, Calculation of activity coefficients, osmotic coefficients, and apparent molal and standard and relative partial molal properties to 600 degrees C and 5kb. *Am. J. Sci.* **1981,** *281* (10), 1249-1516, DOI: 10.2475/ajs.281.10.1249

44.   Andrade, C.; Sanjuán, M. Á., Carbon dioxide uptake by pure Portland and blended cement pastes. *Developments in the Built Environment* **2021,** *8*, 100063, DOI: 10.1016/j.dibe.2021.100063

45.   Burciaga-Díaz, O.; Escalante-García, J. I., Structure, mechanisms of reaction, and strength of an alkali-activated blast-furnace slag. *J. Am. Ceram. Soc.* **2013,** *96* (12), 3939-3948, DOI: 10.1111/jace.12620

46.   Ramachandran, V. S.; Chun-Mei, Z., Thermal analysis of the 3CaO· Al2O3-CaSO4· 2H2O-CaCO3-H2O system. *Thermochim. Acta* **1986,** *106*, 273-282, DOI: 10.1016/0040-6031(86)85139-5

47.   Lothenbach, B.; Durdzinski, P.; De Weerdt, K., Thermogravimetric analysis. In *A practical guide to microstructural analysis of cementitious materials*, CRC press Boca Raton, FL: 2016; pp 177-212.

48.   Santacruz, I.; Torre, Á. G. D. l.; Álvarez-Pinazo, G.; Cabeza, A.; Cuesta, A.; Sanz,

J.; Aranda, M. A. G., Structure of stratlingite and effect of hydration methodology on microstructure. *Adv. Cem. Res.* **2016,** *28* (1), 13-22, DOI: 10.1680/adcr.14.00104

49.   Zajac, M.; Irbe, L.; Bullerjahn, F.; Hilbig, H.; Ben Haha, M., Mechanisms of carbonation hydration hardening in Portland cements. *Cem. Concr. Res.* **2022,** *152*, 106687, DOI: 10.1016/j.cemconres.2021.106687

50.   Thiery, M.; Villain, G.; Dangla, P.; Platret, G., Investigation of the carbonation front shape on cementitious materials: Effects of the chemical kinetics. *Cem. Concr. Res.* **2007,** *37* (7), 1047-1058, DOI: 10.1016/j.cemconres.2007.04.002

51.   Palacios, M.; Puertas, F., Effect of carbonation on alkali-activated slag paste. *J. Am. Ceram. Soc.* **2006,** *89* (10), 3211-3221, DOI: 10.1111/j.1551-2916.2006.01214.x

52.   Andersen, M. D.; Jakobsen, H. J.; Skibsted, J., Incorporation of aluminum in the calcium silicate hydrate (C− S− H) of hydrated Portland cements: A high-field 27Al and 29Si MAS NMR investigation. *Inorg. Chem.* **2003,** *42* (7), 2280-2287, DOI: 10.1021/ic020607b

53.   Andersen, M. D.; Jakobsen, H. J.; Skibsted, J., A new aluminium-hydrate species in hydrated Portland cements characterized by 27 Al and 29 Si MAS NMR spectroscopy. *Cem. Concr. Res.* **2006,** *36* (1), 3-17, DOI: 10.1016/j.cemconres.2005.04.010

54.   Pardal, X.; Brunet, F.; Charpentier, T.; Pochard, I.; Nonat, A., 27Al and 29Si solid-state NMR characterization of calcium-aluminosilicate-hydrate. *Inorg. Chem.* **2012,** *51* (3), 1827-1836, DOI: 10.1021/ic202124x

55.   Wang, S.-D.; Scrivener, K. L., 29 Si and 27 Al NMR study of alkali-activated slag. *Cem. Concr. Res.* **2003,** *33* (5), 769-774, DOI: 10.1016/S0008-8846(02)01044-X

56.   Kumar, S.; Sonat, C.; Yang, E.-H.; Unluer, C., Performance of reactive magnesia cement formulations containing fly ash and ground granulated blast-furnace slag. *Constr. Build. Mater.* **2020,** *232*, 117275, DOI: 10.1016/j.conbuildmat.2019.117275

57.   Li, Q.; Zhang, L.; Gao, X.; Zhang, J., Effect of pulverized fuel ash, ground granulated

blast-furnace slag and CO2 curing on performance of magnesium oxysulfate cement. *Constr. Build. Mater.* **2020,** *230*, 116990, DOI: 10.1016/j.conbuildmat.2019.116990

58.   Shi, D.; Yao, Y.; Ye, J.; Zhang, W., Effects of seawater on mechanical properties, mineralogy and microstructure of calcium silicate slag-based alkali-activated materials. *Constr. Build. Mater.* **2019,** *212*, 569-577, DOI: 10.1016/j.conbuildmat.2019.03.288

59.   Ke, X.; Bernal, S. A.; Provis, J. L., Controlling the reaction kinetics of sodium carbonate-activated slag cements using calcined layered double hydroxides. *Cem. Concr. Res.* **2016,** *81*, 24-37, DOI: 10.1016/j.cemconres.2015.11.012

60.   Rashad, A.; Bai, Y.; Basheer, P.; Milestone, N.; Collier, N., Hydration and properties of sodium sulfate activated slag. *Cem. Concr. Compos.* **2013,** *37*, 20-29, DOI: 10.1016/j.cemconcomp.2012.12.010

61.   Ye, H.; Huang, L.; Chen, Z., Influence of activator composition on the chloride binding capacity of alkali-activated slag. *Cem. Concr. Compos.* **2019,** *104*, 103368, DOI: 10.1016/j.cemconcomp.2019.103368

62.   Skibsted, J.; Henderson, E.; Jakobsen, H. J., Characterization of calcium aluminate phases in cements by aluminum-27 MAS NMR spectroscopy. *Inorg. Chem.* **1993,** *32* (6), 1013-1027, DOI: 10.1021/ic00058a043

63.   Skibsted, J.; Pedersen, M. T.; Holzinger, J., Resolution of the two aluminum sites in ettringite by 27Al MAS and MQMAS NMR at very high magnetic field (22.3 T). *J. Phys. Chem. C* **2017,** *121* (7), 4011-4017, DOI: 10.1021/acs.jpcc.6b11875

64.   Baquerizo, L. G.; Matschei, T.; Scrivener, K. L., Impact of water activity on the stability of ettringite. *Cem. Concr. Res.* **2016,** *79*, 31-44, DOI: 10.1016/j.cemconres.2015.07.008

65.   Ke, X.; Bernal, S. A.; Provis, J. L.; Lothenbach, B., Thermodynamic modelling of phase evolution in alkali-activated slag cements exposed to carbon dioxide. *Cem. Concr. Res.*

2020, *136*, 106158, DOI: 10.1016/j.cemconres.2020.106158

66.   Li, N.; Farzadnia, N.; Shi, C., Microstructural changes in alkali-activated slag mortars induced by accelerated carbonation. *Cem. Concr. Res.* **2017,** *100*, 214-226, DOI: 10.1016/j.cemconres.2017.07.008

For Table of Contents Only:
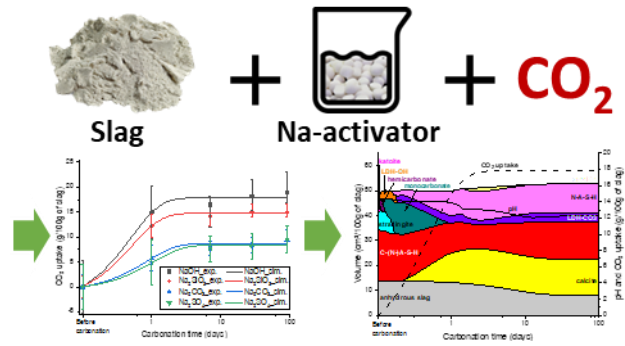
Synopsis

Carbonation of alkali-activated slag activated with four different Na-activators is investigated.